Unveiling the formation and magma transport dynamics of the Ulanqab maar volcanic cluster in the western North China Craton: Insights from ^{40}Ar-^{39}Ar geochronology, mineral chemistry, and Sr-Nd-Mg isotopes

Zong-yuan Tang [a,b], Chen-chang Chen [a,c], Si-ying Gui [d], Jie Li [a,c], De-you Sun [e], Chang-zhou Deng [f], Han Zheng [g], Guo-chun Zhao [h,b,∗]

[a] Hebei Key Laboratory of Strategic Critical Mineral Resources, Hebei GEO University, Shijiazhuang 050031, China
[b] State Key Laboratory of Continental Dynamics, Department of Geology, Northwest University, Xi'an 710069, China
[c] College of Earth Sciences, Hebei GEO University, Shijiazhuang 050031, China
[d] Institute of Environmental Geology, The 7th Institute of Geology & Mineral Exploration of Shandong Province, Linyi, 276006, China
[e] College of Earth Sciences, Jilin University, Changchun 130061, China
[f] State Key Laboratory of Ore Deposit Geochemistry, Institute of Geochemistry, Chinese Academy of Sciences, Guiyang 550081, China
[g] School of Geosciences and Info-physics, Central South University, Changsha 410083, China
[h] Department of Earth Sciences, The University of Hong Kong, Pokfulam Road, Hong Kong, China

ARTICLE INFO

ABSTRACT

The chemical composition of eastern North China Craton (NCC)'s alkaline basaltes likely influenced by subducting Pacific Plate. Nonetheless, the influence of these processes on the western craton remains uncertain due to the lack of geochemical evidence. The recent discovery of Ulanqab maar volcanic cluster (UMVC) in the western NCC has become significant research windows. However, their petrogenesis and magmatic processes remain poorly understood. In the present study, ^{40}Ar/^{39}Ar, whole rock and mineral geochemistry, and Sr-Nd–Mg isotope data for the UMVC in the western NCC are reported. These data reveal that the UMVC was formed during the Neogene (7.60 ± 0.04 Ma), diverging from Quaternary basalts or as part of the Hannuoba basalts (eastern Ulanqab). The UMVC rocks, featuring typical oceanic island basalts traits with moderate (^{87}Sr/^{86}Sr)i values (0.70487–0.70524) and $\varepsilon_{Nd}(t)$ values from −4.95 to + 0.82, likely originated from an enriched EMI-type mantle source during the mid-Proterozoic. This involved mixing melts from 30 to 50 % partial melting of garnet lherzolite and 5–15 % partial melting of garnet pyroxenite in a deep magma chamber. Crystallization of clinopyroxene and garnet in this chamber created high-Ti alkaline lavas, with limited presence in erupted lavas due to sluggish magma ascent in the profound lithospheric mantle. In shallower lithospheric mantle regions, interactions between alkaline magma and orthopyroxenite improved transport kinetics, enabling clinopyroxene and olivine crystallization under lower pressure. These magmas integrated mafic crystal mushes from accumulation chambers. The study also identified a low Mg isotope composition (δ^{26}Mg = − 0.56 ‰ to − 0.42 ‰) in samples, suggesting a hybrid source influenced by early decarbonation in Precambrian subduction zones. This finding indicates the incorporation of Mg-rich carbonate minerals from marine sediments into the magma source, contributing to the observed variations in eastern China's alkaline basalts.

1. Introduction

Oceanic island basalt (OIB) is renowned for its association with enriched magmas derived from mantle plumes or hot spots, characterized by temperatures that surpass those of the ambient mantle by 100–300 °C (e.g., White, 2010). While peridotite is commonly considered a dominant source lithology, recent studies suggest significant contributions from ultramafic metasomatites such as carbonated peridotite, pyroxenite, and hornblendite to the origin of alkali basalts (Dai et al., 2017; Herzberg, 2011; Tan et al., 2022; Zeng et al., 2010). Elucidating the mantle sources of OIB basalts assumes paramount importance in unraveling their petrogenesis and the underlying processes within oceanic islands. This raises a fundamental inquiry regarding the role of ultramafic

∗ Corresponding author.
    E-mail address: gzhao@hku.hk (G.-c. Zhao).

metasomatites in the origin of OIB basalts, necessitating further exploration of their contributions.

The generation of OIB alkaline magmas has sparked intense discussions regarding its precise origin. Potential origins include: a mantle plume (Hofmann, 1997), subduction of an oceanic slab (Xu and Zheng, 2017), and the recycling of crustal components similar to stagnated sandwich structures in the asthenosphere (Blichert–Toft et al., 1999). Extensive research has focused on investigating OIB sources within the context of the North China Craton (NCC) and its associated enriched mantle I (EM-I) type lithospheric mantle (Peng et al., 2007; Zhai et al., 2011; Tang et al., 2022). One of the notable mantle sources contributing to OIB magmas is the result of partial melting of eclogite or pyroxenite formations (Dasgupta et al., 2006; Huang and Frey, 2005; Kogiso and Hirschmann, 2006; Ren et al., 2005; Sobolev et al., 2005, 2007). Therefore, comprehending the nature and provenance of peridotite and/or pyroxenite in the mantle source, assumes paramount importance in resolving these scientific controversies and attaining profound insights into the mechanisms governing intraplate volcanism.

In addition, the subducted Pacific Oceanic Plate has been a subject of understanding the origins of continental intraplate basalts in the NCC. Recent seismic imaging studies have revealed the subducted Pacific Oceanic Plate extends towards the northern segment of the North-South Gravity Lineament (NSGL; Zhao, 2021) in the NCC region. However, the role of Pacific slab-derived materials in the origin of intraplate basalts in the western NSGL and their contribution to the elemental and isotopic compositions remain uncertain (Yang et al., 2012; Zou et al., 2008). Hence, the detection and analysis of carbonates within basaltic sources represent a pivotal aspect for gaining valuable insights into the mechanisms influencing intraplate volcanism. In this regard, the utilization of magnesium (Mg) isotope data is of utmost importance (cf. Liu and Li, 2019). By analyzing Mg isotope signatures, researchers can identify potential components within the deep mantle, shedding light on the complex processes that govern the origin and evolution of intraplate basalts.

In this study, we aim to illuminate the origin and evolution of OIB-type alkaline magmas, with a particular focus on the Ulanqab maar volcanic cluster (UMVC) in the western NCC. To achieve this, we use a comprehensive set of analytical techniques, including ^{40}Ar–^{39}Ar geochronology, whole rock geochemistry, major elements analysis of olivine and clinopyroxene, and Sr–Nd–Mg isotope data. Our study highlights a multistage magma evolution model. The UMVC exhibits an enriched mantle source, possibly linked to garnet pyroxenitic and garnet lherzolitic sources. Additionally, the incorporation of Mg-rich carbonate minerals from marine sediments suggests a complex interaction during magma formation. This multistage process involves crystallization of clinopyroxene and garnet in deep magma chambers and subsequent magma transport and interaction with orthopyroxenite in the shallower lithospheric mantle, leading to the crystallization of clinopyroxene and olivine.

2. Geological setting

The NCC, crystallized approximately 3.8 Ga, constitutes the most ancient basement structure in China and is regarded as one of Earth's most archaic cratons (Liu et al., 1992a). The NCC is bifurcated into a Western Block (WB) and an Eastern Block (EB) by the Trans-North China Orogen (TNCO) (Fig. 1). These two discrete blocks amalgamated circa 1.85 Ga, consummating the formation of the unified NCC landmass (Zhao et al., 2000). Dating back to the Mesozoic (~0.25 Ga), the lithosphere associated with the NCC experienced thinning, accompanied by extensive

tectono–thermal events (Xu et al., 2009). Geophysical data has provided evidence of a significant reduction in lithospheric thickness beneath the NCC, particularly in the eastern sector situated east of the NSGL (Fig. 1b). In contrast, the western NCC, especially within the Ordos Basin, where Archean to Paleoproterozoic basement have been remarkably preserved (Fig. 1b; Zhu et al., 2012). Progressive lithospheric mantle thinning transpired in an eastward trajectory across the NCC, engendering a transition from a cold, thick (~200 km), and highly refractory to a hot, thin (~80 km), and enriched young oceanic lithospheric mantle (Wu et al., 2003). Located in the western NCC, the Cenozoic Ulanqab maar volcanic cluster (UMVC) exists as an example of an intraplate setting (Fig. 2). Analysis of this UMVC may elucidate Cenozoic maar volcanism within the backdrop of the NCC's ancient lithosphere.

In eastern China, Cenozoic intraplate basalts are primarily located within rift and fault basins adjacent to significant regional faults, such as the NSGL and Tanlu and Yilan–Yitong faults (Fig. 3a; Wu et al., 2020). Continental intraplate volcanism was widespread in eastern China during Cenozoic times (e.g., Liu, 1999). Over time, the composition of Cenozoic intraplate basalts in eastern China has exhibited distinct variations. The Paleogene basalts are dominantly tholeiites, with sporadic occurrences of alkaline basalts, predominantly present in the eastern NCC and Songliao Basin (Fig. 3a). Transitioning into the Neogene period, alkaline basalts became more prominent, particularly along the continental margin of southeastern China and along the Tan-Lu, Yilan–Yitong, and Dunhua–Mishan fault zones (Tian et al., 1992). In contrast, the western NCC features both alkaline basalts and tholeiites in the form of the Neogene Hannuoba basalts (Zheng, 1985). In the Quaternary period, eastern China witnessed the emergence of scattered Quaternary alkali basalts and tholeiites, primarily exposed in regions such as the Leiqiong Peninsula, eastern NCC, and northeastern China. Notably, the Quaternary volcanoes within the Northeast China and North China Rift System are spatially concentrated in its outermost rim, with a gradual decrease in volcanic activity intensity observed since the Middle Pleistocene (Tian et al., 1992).

Shifting our focus to the Ulanqab area, we find a geological basement predominantly composed of Archean metamorphic rocks and Permian granites (Fig. 4). The UMVC was assigned to the Quaternary based on stratigraphy (Bai et al., 2020), whereas K–Ar dating (25–14 Ma; Liu et al., 1992b) suggests that it belongs to the Neogene (Hannuoba basalts). Within the Ulanqab maar volcanic cluster, craters manifest predominantly as circular or ovoid negative topographic features (Fig. 5a, c, and e), comprised chiefly of lava flows. The rocks contain mainly olivine (10–15 vol%) and clinopyroxene (<5 vol%) phenocrysts and comprise plagioclase, olivine, clinopyroxene, and titanomagnetite in a matrix, producing intergranular or pilotaxitic textures (Fig. 5b, d, and f). Clinopyroxene phenocrysts sometimes exhibit growth zonation and hourglass textures (Fig. 5b), whereas olivine primarily occurs as millimetric euhedral to subhedral crystals.

3. Analytical methods

3.1. Ar–Ar geochronology

^{40}Ar/^{39}Ar analyzes were performed in the laboratory of the Beijing Research Institute of Uranium Geology. Plagioclase obtained from matrix of the basalt (Ma-14) was crushed to the 40–60 mesh size range, and each sample was wrapped in aluminum foil. Samples were then sealed in quartz tubes coated with 1 mm thick cadmium, and these were shipped to the China Institute of Atomic Energy Science, where irradiation was conducted for 24 h using a fast neutron reactor. Details on the analytical methods and the ^{40}Ar/^{39}Ar data for samples are presented in Table S1.
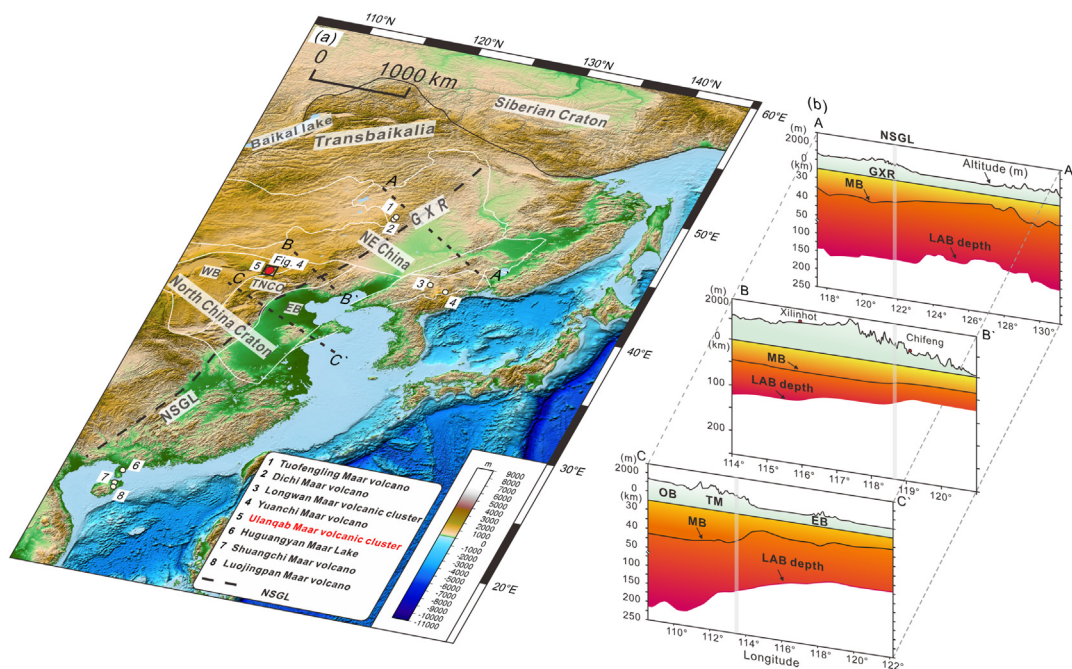
Fig. 1. (a) Distribution of the maar volcanoes in eastern China. (b) Altitude, crust-mantle boundary, and lithosphere-asthenosphere boundary depth along three profiles through Northeast China and North China, respectively (modified from Guo et al., 2020; Zhang et al., 2018). Abbreviation: EB = Eastern Block; GXR = Great Xing'an Range; LAB = Lithosphere-asthenosphere boundary; MB = Moho boundary; NSGL = North-South Gravity Lineament; OB = Ordos Basin; TM = Taihang Mountains; TNCO = Trans-North China Orogen; WB = Western Block.
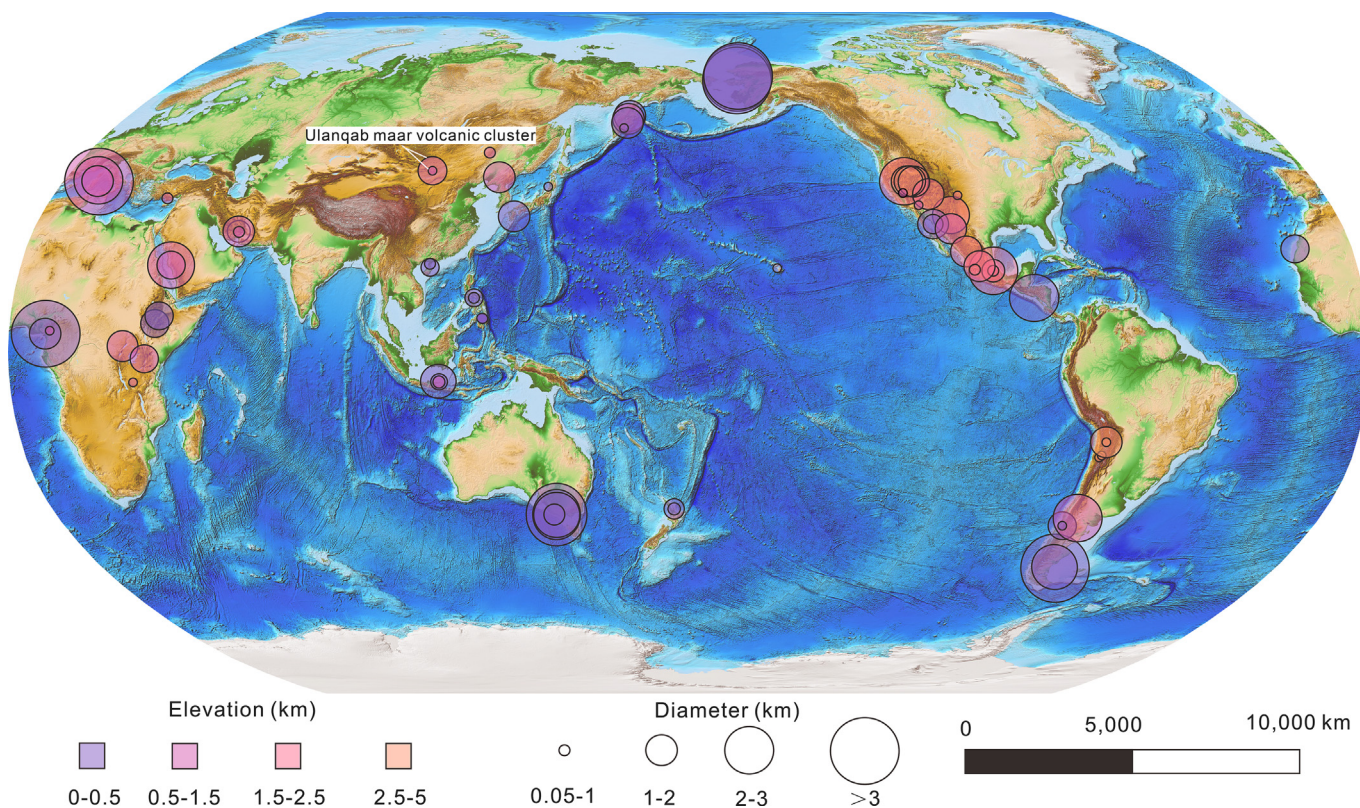

Fig. 2. Distribution of the main maar volcanoes on Earth showing crater elevation and diameter on earth (after Graettinger, 2018).

3.2. Electron–probe microanalysis (EPMA)

The compositions of major elements in olivine and clinopyroxene from samples were determined using a JXA-8230 electron microprobe in the Hebei Key Laboratory of Strategic Critical Mineral Resources, Hebei GEO University, Shijiazhuang, China. The equipment was operated using an acceleration voltage of 15 kV, a beam current of 20nA, and a spot size with a diameter of 1 μm.
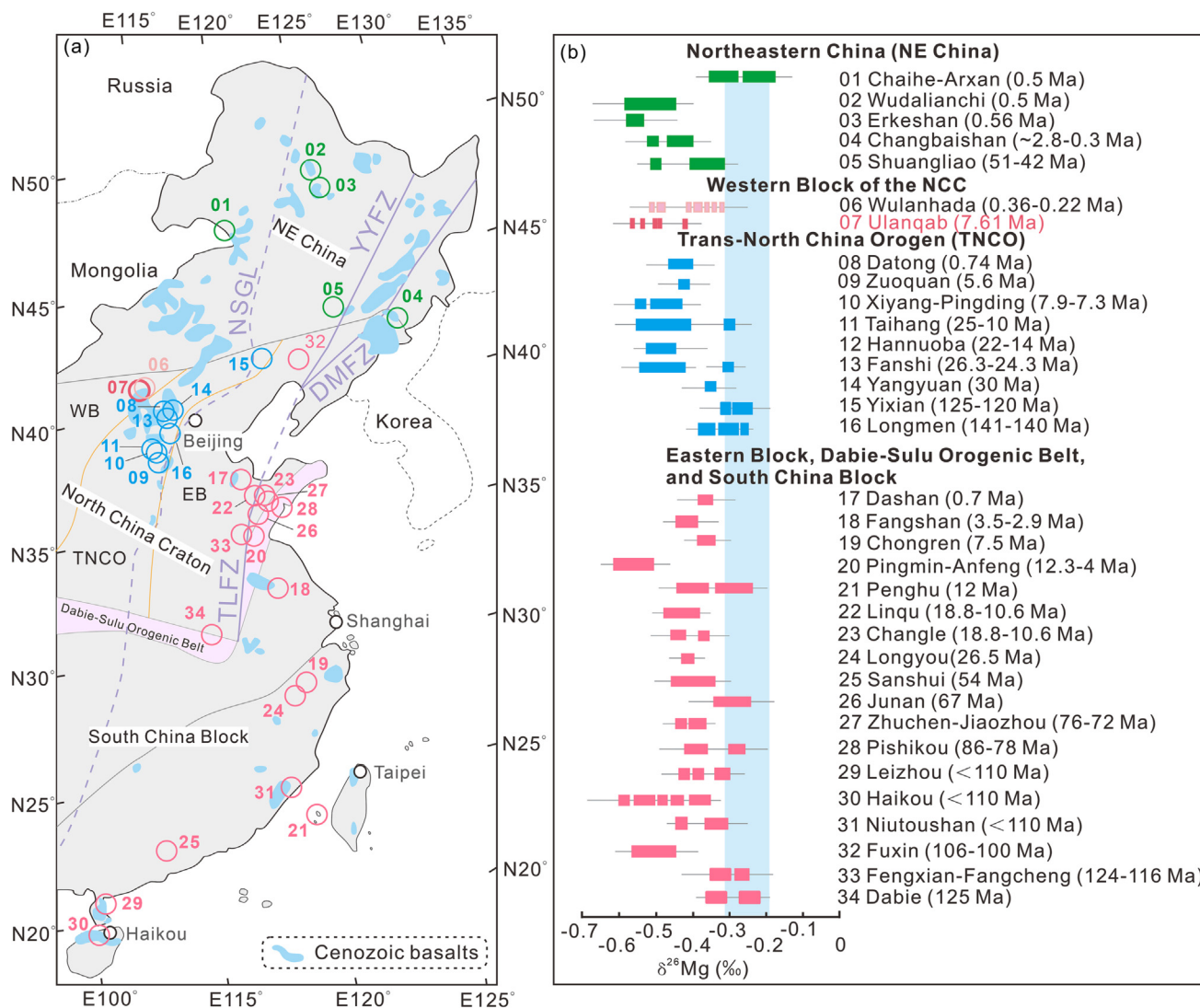
Fig. 3. (a) Schematic map of eastern China (modified from Li et al., 2017; Dong et al., 2019). (b) $\delta^{26}Mg$ variations of basaltic samples from 34 locations (data from Li et al., 2017 and references therein; Su et al., 2017; Sun et al., 2021; Tian et al., 2016 and references therein). The ice blue bar represents the average mantle ($\delta^{26}Mg = -0.25 \pm 0.07$, Teng et al., 2010). Abbreviations: TLFZ = Tan-Lu Fault Zone; DMFZ = Dunhua–Mishan Fault Zone; YYFZ = Yilan–Yitong Fault Zone; NSGL = North-South Gravity Lineament; WB = Western Block; TNCO = Trans-North China Orogen; EB = Eastern Block. (For interpretation of the references to colour in this figure legend, the reader is referred to the web version of this article.)

The peak and background counting times on each side of a peak were 10 and 5 s, respectively. The Phi–Rho–Z method was used to identify and integrate peaks, and this involved a background subtraction, followed by calculation of the concentrations of elements in the minerals (Mondal et al., 1994). The calibration and EPMA data for samples are presented in Tables S2 and S3.

3.3. Major and trace element analyzes

Twenty-two samples were pulverized to the < 200 mesh size, and these were analyzed using whole rock geochemistry in ALS Chemex (Guangzhou, China). Major elements were analyzed after fusion by inductively coupled plasma–atomic emission spectroscopy using a P61-XRF26s instrument and by X-ray fluorescence spectroscopy. Trace elements were determined by inductively coupled plasma-mass spectrometry (ICP–MS) using an M61-MS81 instrument, according to the method described on the website of ALS Chemex. Certified reference materials including SARM-4, OREAS-120, and GBM908-10 were analyzed with each batch to ensure accuracy and precision of the analyzes. The analytical

uncertainty based on the reference materials was better than 5 % for major elements and 10 % for trace elements. The major and trace element compositions of the UMVC samples and reference materials are presented in Table S4.

3.4. Whole rock Sr–Nd isotope analyzes

Whole rock Sr–Nd isotope analyzes were performed in the laboratory of the Beijing Research Institute of Uranium Geology. Sr isotopes were measured using thermal ionization mass spectrometry (TIMS) involving single Re filaments and a Ta activator. The TIMS was performed using a Phoenix spectrometer equipped with nine Faraday sensors and a Daly detector. The data generated were corrected for internal mass bias to $^{86}Sr/^{88}Sr = 0.1194$. The instrument drift was corrected using NBS 987 (0.710229 ± 13) as an external standard, and all measurements were performed in the static mode. The ^{87}Rb interference was corrected by monitoring ^{85}Rb using an $^{85}Rb/^{87}Rb$ factor of 2.5926. Nd isotopes were measured using TIMS with triple Re filaments in the static mode. The TIMS was performed using an ISOPROBE_T spectrometer equipped
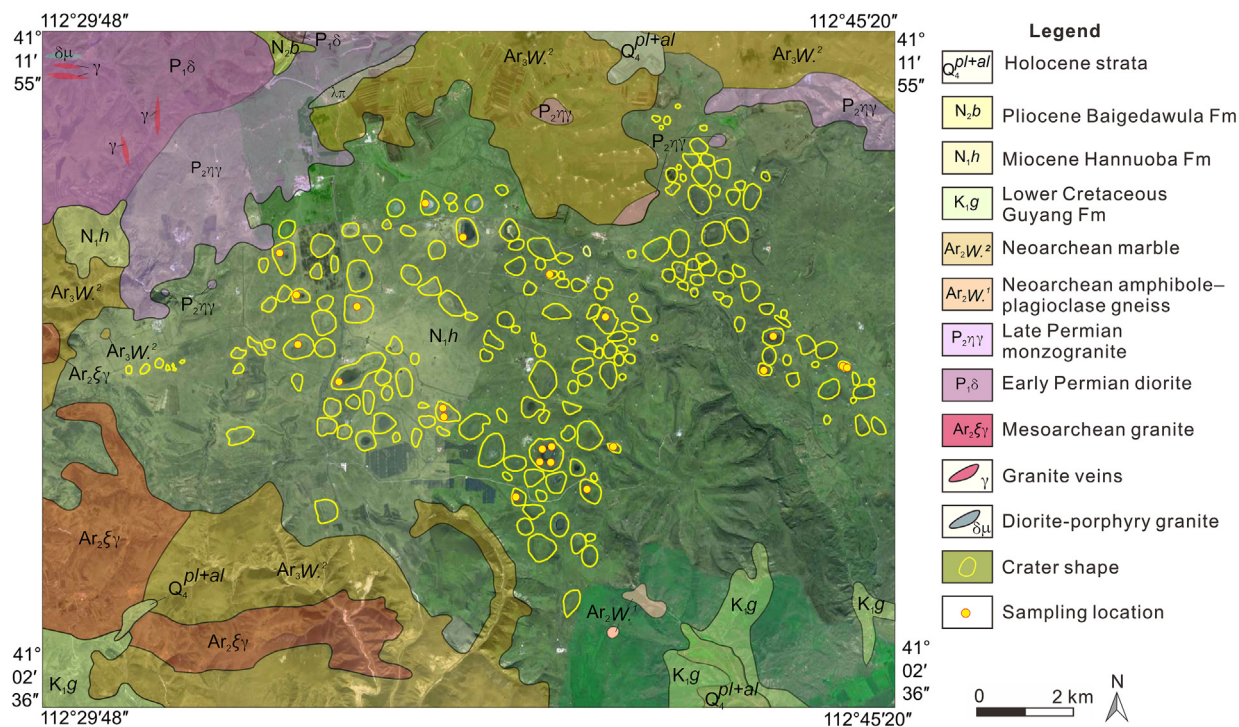
Fig. 4. Simplified geological map of the Ulanqab maar volcanic cluster showing sample localities.

with nine Faraday sensors and an ETP detector. The data were corrected for internal mass bias to an $^{144}Nd/^{146}Nd$ factor of 0.7219 using an exponential fractionation expression. The instrumental drift was corrected using JNdi-1 (0.512109 ± 3) as an external standard (Tsuyoshi Tanaka et al., 2000), and the Sr–Nd isotope compositions of samples are presented in Table S5.

3.5. Whole rock Mg isotope analyses

Magnesium (Mg) isotopes in samples were analyzed in the Beijing Createch Testing Technology Co., Ltd. The Mg isotope ratios for samples were determined using a multi-collector ICP–MS (MC–ICP–MS), and separation of Mg isotopes was achieved using the cation resin AG 50 W-X12 (200–400 mesh, Bio-Rad). Details on the operation of the equipment and the analytical conditions are available in An et al. (2014). The Mg isotope compositions of samples and reference materials are presented in Table S6.

4. Results

4.1. Ar–Ar dating

Ar–Ar data for plagioclase (Ma-14) shows a concordant age spectrum (Fig. 6a and Table S1). Six consecutive steps in the spectrum account for 83.81 % of the total ^{39}Ar released, and these produced a plateau age of 7.60 ± 0.04 Ma (MSWD = 1.61; Fig. 6a). This age is consistent with the 7.61 ± 0.06 Ma (MSWD = 2.01; Fig. 6b) of an inverse isochron, which can be calculated from the six steps. The $^{40}Ar/^{39}Ar$ spectra age [$(^{40}Ar/^{36}Ar)_{initial}$ = 294.8 ± 7.4] and the atmospheric $^{40}Ar/^{36}Ar$ intercept value of 295.5 indicate that there was no resolvable excess argon contamination. Therefore, the plateau age of 7.60 ± 0.04 Ma is the probable age of the UMVC.

4.2. Mineral chemistry

Analyses of 81 points in olivine samples produced Fo values [molar 100 × Mg / (Mg + Fe^{2+})] that vary from 77 to 83. The Ni and Mn concentrations of the olivine samples yielded concentration ranges of 487–2239 ppm and 1055–1991 ppm, respectively (Fig. 7a and b; Table S2). The NiO concentrations of olivine samples in the present study are comparable to those of Hawaiian olivine but different from those of mantle olivine (Fig. 7c; Sato, 1977).

Regarding clinopyroxenes, 37 points were analyzed in each sample, and based on the compositions (Wo$_{41.29–46.36}$, En$_{39.84–45.83}$ and Fs$_{9.74–12.78}$; Table S3), these can be categorized as diopside and augite (Fig. S1a). The Mg# of the clinopyroxene samples produce a range of 79.61–86.12, whereas the ranges of concentrations for CaO, Al$_2$O$_3$, TiO$_2$, and Na$_2$O are correspondingly 19.82–22.02, 2.78–6.34, 0.78–2.28, and 0.4–0.6 wt% (Table S3).

4.3. Major and trace element compositions

In the total alkali–silica (TAS) (Fig. 8a) and Ti/Y versus MgO (Fig. 8b) diagrams, data for all 22 samples plot in the area assigned to alkaline and basalts. These alkaline basalts exhibit limited SiO$_2$ (47.32–50.93 wt%), TFe$_2$O$_3$ (11.06–12.98 wt%), and TiO$_2$ (2.09–2.42 wt%) contents with some variations in MgO (4.82–7.63 wt%) and K$_2$O + Na$_2$O (4.68–5.75 wt%).

The samples display light and heavy rare earth element (LREE and HREE, respectively) enrichment patterns typical of the OIB, with LREE/HREE and (La/Yb)$_N$ ratios of 5.74–9.55 and 7.93–17.87, respectively, as well as weak positive Eu anomalies (δEu = 0.93–1.08) (Fig. 9a). In addition, the samples are enriched in large ion lithophile elements (LILE), such as Ba, Sr, and K, and show no significant depletion in high field strength elements (HFSEs). These characteristics are similar to those of normal OIBs but are distinct from those of the HIMU-type (high μ, μ=$^{238}U/^{204}Pb$) OIBs (Fig. 9b).

Fig. 5. Representative photographs (a, c, and e) and photomicrographs (b,d, and f) of the Ulanqab maar lavas (olivine basalts). Abbreviations: Cpx = clinopyroxene; Ol = olivine; Pl = plagioclase; Idn = iddingsite; Kfs = K-feldspars.
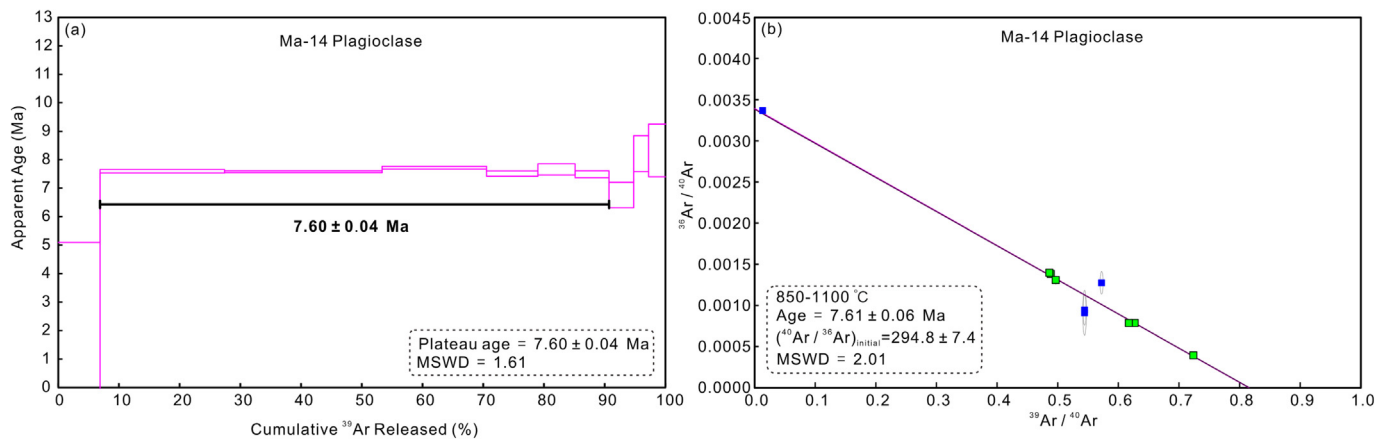

Fig. 6. $^{40}Ar/^{39}Ar$ age spectra (a) corresponding inverse isochron (b) plots of plagioclase from sample Ma-14. The plateau ages are indicated by the bold black. The solid green square denotes the steps used in fitting inverse isochron. The solid blue square does not participate in the calculation of plateau age. 1 sigma errors are quoted for the points plotted in isotope correlation diagrams. (For interpretation of the references to colour in this figure legend, the reader is referred to the web version of this article.)
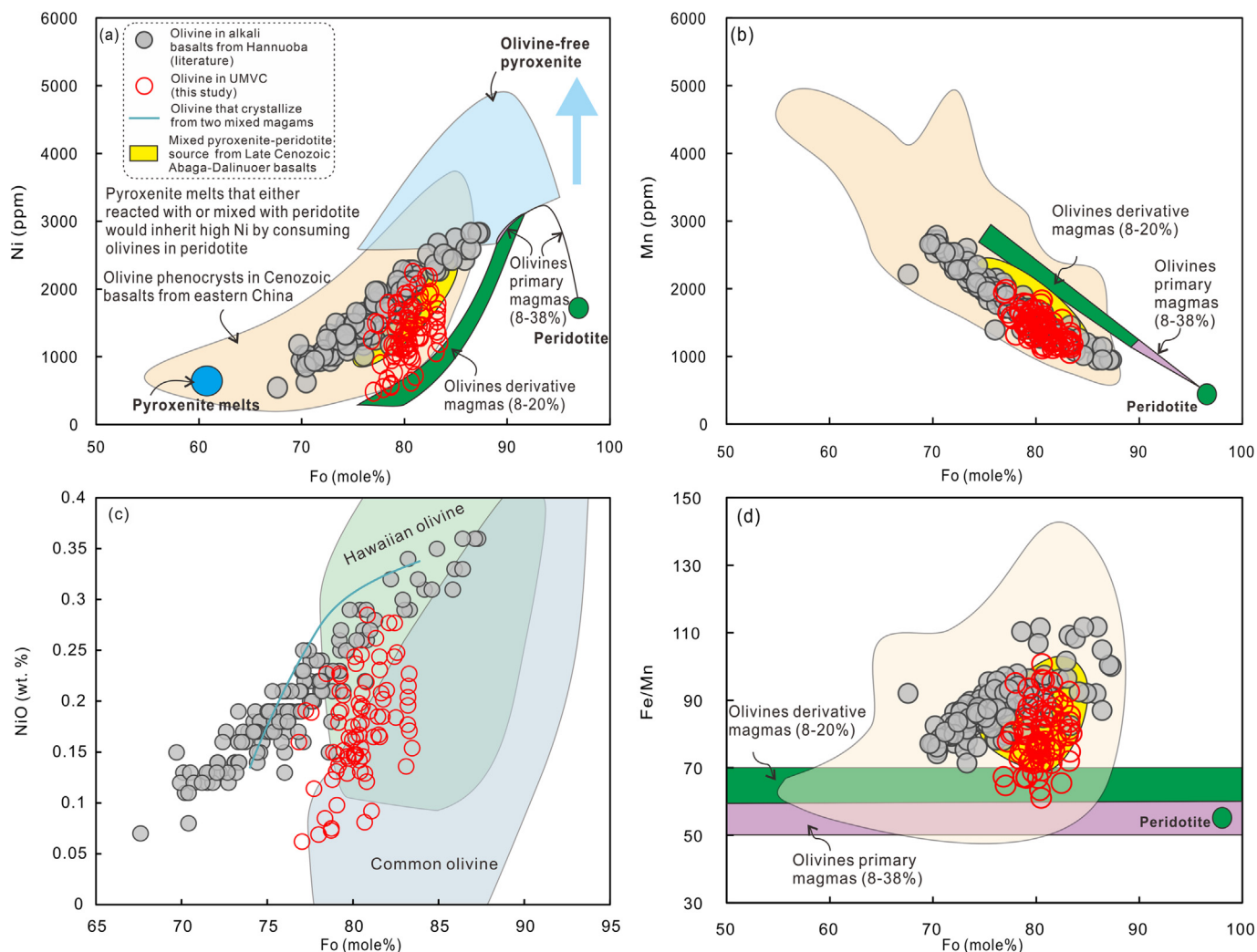
Fig. 7. Plots of olivine for the Ulanqab maar volcanic cluster. (a) Fo (mole%) versus Ni (ppm); (b) Fo (mole%) versus Mn (ppm); (c) Fo (mole%) versus Fe/Mn and (d) Fo (mole%) versus NiO (wt.%). The "common olivine" field is from Sobolev et al (2005) based on olivine in mantle xenoliths, oceanic abyssal peridotites and mid-ocean-ridge basalts, orogenic massifs and ophiolites, while the Hawaiian olivine field outlines the range for olivine from Hawaiian basalts (Sobolev et al., 2005). The green curve is from Qian et al. (2015). Data source for pyroxenite melts, peridotite, olivine-free pyroxenite are from Herzberg (2011). Olivine phenocrysts in Cenozoic basalts from eastern China are based on Zhang and Guo (2016) and references therein. Alkali basalts from Hannuoba are from Zou et al. (2022) and references therein. (For interpretation of the references to colour in this figure legend, the reader is referred to the web version of this article.)

4.4. Whole-rock Sr–Nd isotope composition

The $(^{87}Sr/^{86}Sr)_i$ ratios obtained from analyzes of 10 samples range from 0.70487 to 0.70524, and the corresponding $^{143}Nd/^{144}Nd$ ratios and $\varepsilon_{Nd}(t)$ values vary from 0.512400 to 0.512677 and from − 4.95 to + 0.82 (Fig. 10). The single-stage depleted mantle model ages (T_{DM1}) produced a range of 1.02–1.51 Ga.

4.5. Whole rock Mg isotope composition

Six basalt samples from Ulanqab yielded $\delta^{26}Mg$ values (−0.56 ‰ to − 0.42 ‰ with a mean of − 0.49 ‰) that are lower than those of depleted normal mid-ocean ridge basalts (N-MORB, $\delta^{26}Mg$ = − 0.25 ‰ ± 0.06 ‰; Fig. 3b; Teng et al., 2010). As shown in the $\delta^{25}Mg$ versus $\delta^{26}Mg$ plot (Fig. S2), data for these samples are near the equilibrium isotope fractionation region, and the associated slope of 0.521 highlights the precision of the Mg data.

5. Discussion

The chemical index of alteration (CIA) values for the samples (Table S4; 36.71–44.83) are consistent with those for unaltered

basalts (30–45; Nesbitt and Young, 1982). The weak correlations between data for elements that are mobile in fluids (e.g., K and Ba) and the loss on ignition (LOI) confirm that the samples analyzed were also not affected by significant alteration (Fig. S3a and b; Fan et al., 2014).

The ratios of incompatible elements in the analyzed samples, such as Nb/U (30–––121; mean = 58), are significantly higher than those found in average continental rocks (8; Rudnick and Fountain, 1995). Moreover, no correlations are observed between the $^{87}Sr/^{86}$-Sr ratios and $\varepsilon_{Nd}(t)$ values (Fig. S3c and d). Similarly, $\varepsilon_{Nd}(t)$ values also exhibit no correlation with Ti/Y ratios, and there is no correlation between $\delta^{26}Mg$ and LOI data (Fig. S3e and f). These results indicate a negligible influence of crustal assimilation on the UMVC.

Generally, crystal fractionation of silicate minerals in basaltic magmas does not lead to Mg isotopic fractionation (Teng et al., 2010). The low $\delta^{26}Mg$ values and MgO concentrations demonstrate that the Mg isotope fractionation associated with silicate fractionation was insignificant in the analyzed samples (Fig. S4a; Teng et al., 2010). In this study, the $\delta^{26}Mg$ data exhibit no clear relationship with V, Cr, and TiO_2 (Fig. S4b, c, and d), suggesting that fractionation of chromite and Fe – Ti – Cr spinel minimally influenced the measured low $\delta^{26}Mg$ values (Su et al., 2019).
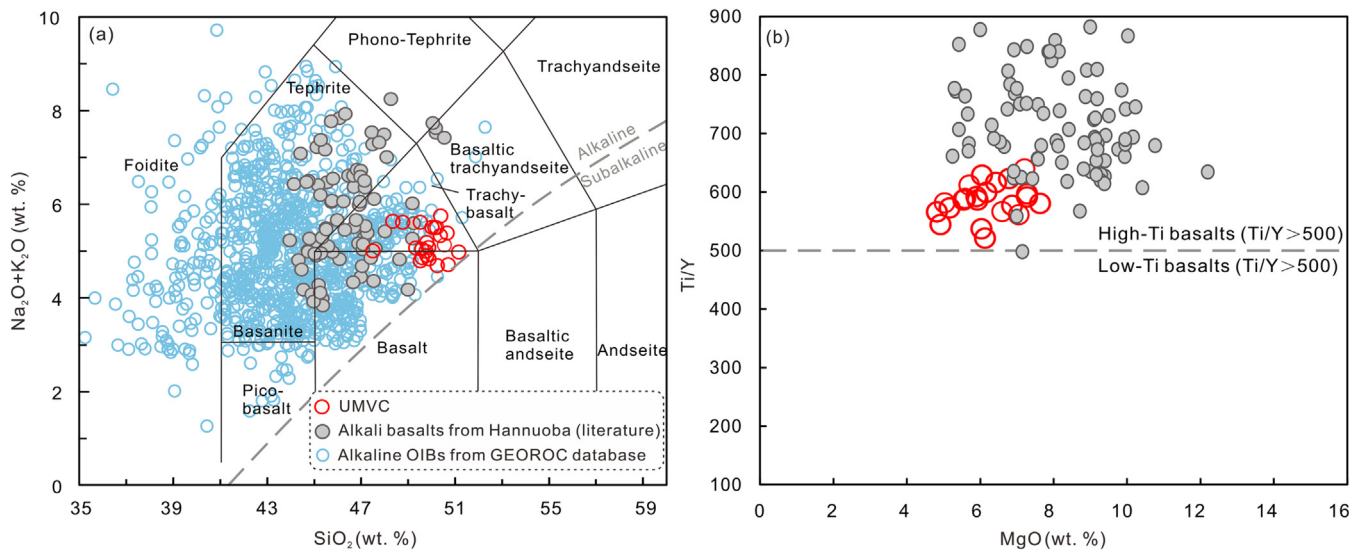
Fig. 8. Plots for (a) SiO₂ (wt. %) versus (Na₂O + K₂O) (wt. %) (after Irvine and Baragar, 1971) and (b) Ti/Y versus MgO (after Yang and Liu, 2019) of the Ulanqab maar lavas. OIBs are from GEOROC database. Alkali basalts from Hannuoba are from Zou et al. (2022) and references therein.
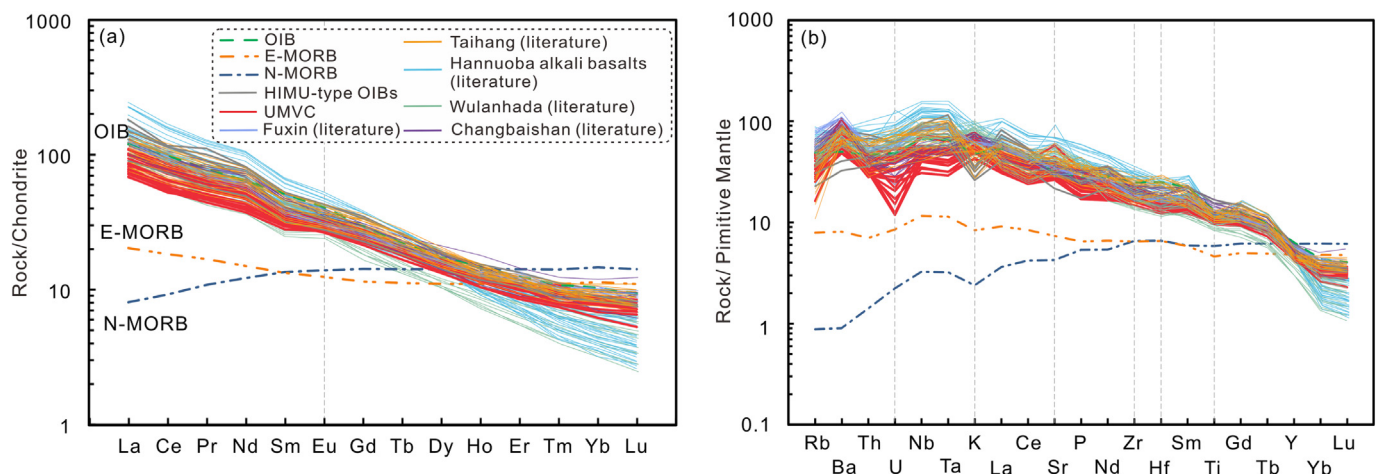

Fig. 9. Plots of Chondrite-normalized REE patterns (a) and primitive-mantle-normalized multi-element variations (b) for the Ulanqab maar lavas. Data source: OIB, E-MORB and N-MORB are from Sun and McDonough (1989); HIMU-type (high μ, μ=^{238}U/^{204}Pb) and OIBs are from Huang and Zheng (2017). Chondrite values are from Boynton (1984), and primitive mantle values are from Sun and McDonough (1989). Data for Hannuoba alkali basalts are from Zou et al. (2022) and references therein; Data for Wulanhada basalts are from Zhao et al. (2019); Data for Chnagbaishan basalts (~2.8–0.31 Ma) are from Tian et al. (2019); Data for Taihang basalts (26–6 Ma) and Fuxin basalts (106–100 Ma) are from Li et al. (2017).

Moreover, the TiO₂ concentrations (2.09–2.42 wt%) of the Ulanqab basalt samples are evidently lower than those of high-Ti lunar basalts (>6 wt%; Sedaghatpour et al., 2013), indicating the absence of significant ilmenite accumulation in the mantle source of the basalts. The δ^{26}Mg values of pyroxenite- and peridotite-derived melts are also higher than values for samples from the UMVC (Fig. S5). Therefore, the low-degree partial melting of peridotite or pyroxenite cannot fully account for the low δ^{26}Mg values of the samples analyzed (cf. Zhong et al., 2017). In summary, the low δ^{26}Mg values of samples from the UMVC cannot be explained completely by crystal fractionation and low-degree partial melting an isotopically light mantle source component is required.

5.1. Mantle source composition

The UMVC is characterized by an OIB-like trace element composition, which involves enrichments in LILE and LREE (Fig. 9). Its Sr–Nd isotope composition is associated with high Sr isotope ratios and variable $\varepsilon_{Nd}(t)$ values (Fig. 10). These alkaline basalt characteristics can be attributed to an enriched EMI-like mantle. According to experimental petrology data, (garnet) pyroxenite, hornblendite, and carbonated peridotite (peridotite + CO₂), carbonated pyroxenites and pyroxenite-peridotite mixed sources can serve as parental magmas of alkaline basalts (Chen et al., 2009; Dasgupta et al., 2007; Gómez-Ulla et al., 2018; Søager et al., 2015). Magma formed from the presence of carbonated mantle exhibits evident negative Ti, Zr, and Hf anomalies (Zeng et al., 2010), which is consistent with primitive mantle-normalized patterns of the UMVC samples (Fig. 9). However, the presence of high TiO₂ contents (>2 wt%; Fig. 11a) and Al₂O₃ contents (13.94–15.78 wt%; Fig. 11b), in conjunction with low MgO and CaO contents (Fig. 11c), as well as the absence of negative K anomalies and high Zr/Hf ratios (Fig. 9) within the primary magmas of UMVC, suggests that a carbonated peridotite source is unlikely. Additionally, the trace element characteristics of the UMVC samples differ significantly from those of melts formed by partial melting of metasomatized hornblendite
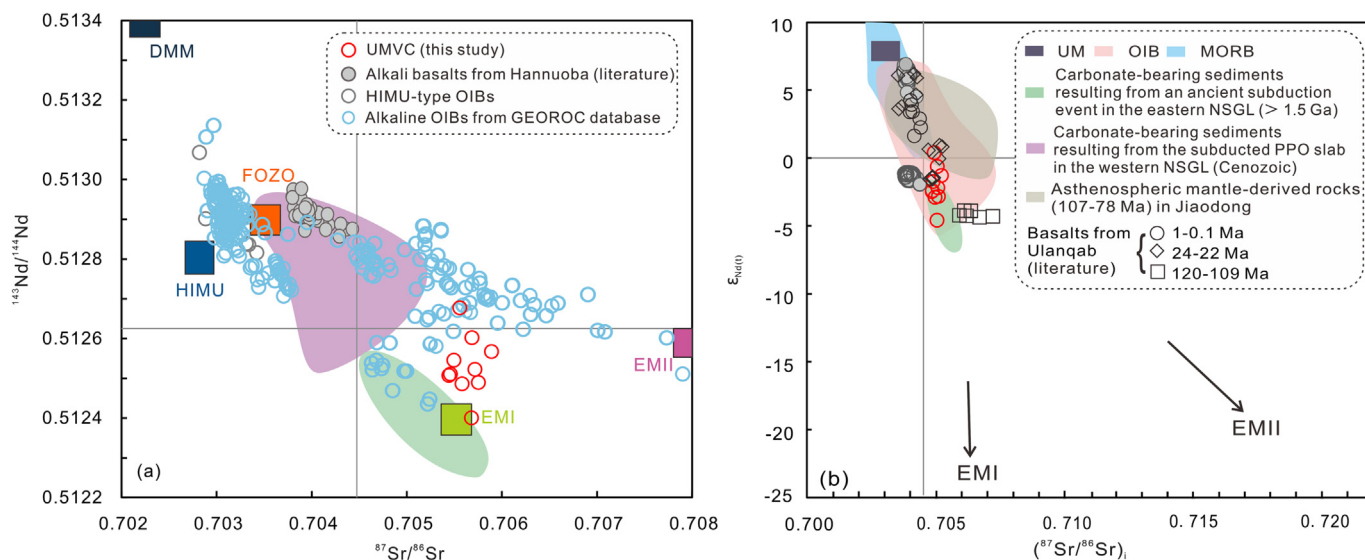
Fig. 10. Diagram of (a) $^{143}Nd/^{144}Nd$ versus $^{87}Sr/^{86}Sr$ (b) $\varepsilon_{Nd}(t)$ vs. $(^{87}Sr/^{86}Sr)_i$ for the Ulanqab maar lavas. Data sources are same as in Fig. 7. Abbreviations: DMM = depleted mid-ocean ridge basalt mantle, EMI = (Enriched Mantle 1), EMII = (Enriched Mantle 2), HIMU = high $^{238}U/^{204}Pb$ mantle, FOZO = Focus Zone, NSGL = North–South Gravity Lineament, PPO slab = Paleo–Pacific oceanic slab. The literature data for 120–109 Ma, 24–22 Ma, 1–0.1 Ma basalts from Ulanqab are from Guo et al. (2014) and references therein. Data for DM, EMI and EMII are from Zindler and Hart (1986). Asthenospheric mantle-derived mafic rocks (107–78 Ma) are from Ma et al. (2014). Isotopic compositions of the mantle end-members are taken from Chen et al. (2007). Carbonate-bearing sediments resulting from an ancient subduction event in the eastern NSGL (> 1.5 Ga) are from Sun et al. (2021), Tian et al. (2016), and Wang et al. (2017).
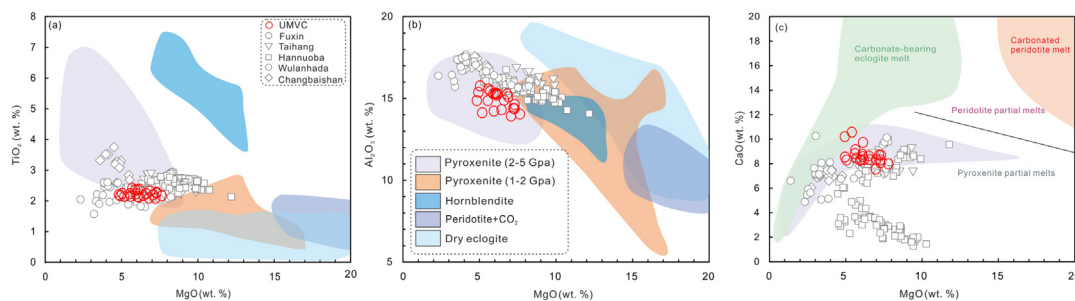

Fig. 11. Plots of the Ulanqab maar lavas with the high-pressure experimental partial melts of various ultramafic rocks: (a) TiO_2 versus MgO, (b) Al_2O_3 versus MgO, and (c) CaO versus MgO. Data sources are the same as Herzberg (2011) and references therein. Data are same as in Fig. 9.

veins. These melts exhibit notable positive anomalies in Nb, Ta, and Ti, as well as negative anomalies in Zr, Hf, and K (Fig. 9; Pilet et al., 2008). These discrepancies indicate the need to explore alternative magma sources.

Given the intricate nature of determining the mantle source for UMVC, it is crucial to take into account a comprehensive array of clues and evidence, especially those related to the minerals present. The olivine Ni-Fo diagram (Fig. 7a and c) suggests that a mantle source consisting solely of peridotite is unlikely to fully explain the observed trend. This is because highly magnesian olivines (Fo > 85) would not be expected to fractionate from all ascending magmas. Furthermore, additional evidence supports the idea of pyroxenite-derived melts as the magma source. The $\delta^{26}Mg$ versus TiO_2 plot (Fig. S4d) and low La/Nb values (0.61–0.97, Stracke and Bourdon, 2009) for the samples studied provide support for this. Moreover, the low Ni content of olivine (487–2239 ppm) in the UMVC argues against a single olivine-free pyroxenite melt as the source (Fig. 7a; Herzberg, 2011). Furthermore, the direct partial melting of peridotite cannot yield UMVC olivine magma with low Mn contents (Fig. 7b; Salters and Stracke, 2004). As a result, an alternative explanation for the presence of olivine with such characteristics becomes necessary. One plausible explanation for the presence of olivine with low Mn content in the UMVC magma lies

in the involvement of pyroxene. This hypothesis support from the elevated Fe/Mn ratio observed in the UMVC olivine (Fig. 7d). The high Fe/Mn ratio is commonly attributed to the stability of Mn content during the formation of magma in a garnet-rich source. Additionally, the UMVC samples yielded high $(La/Yb)_N$ (7.92–17.87) and Dy/Yb (2.55–3.65) ratios, as well as low Y concentrations, which imply a garnet residual in the source (Shaw et al., 2003). Further support for this hypothesis comes from quantitative modeling of melt compositions (Fig. 12), which delineates partial melting trajectories involving varying proportions of partially melted garnet pyroxenite (5–15 %) and partially melted garnet lherzolite (30–50 %). These findings indicate the involvement of a deep mantle source, specifically a garnet lherzolite melt, in the formation of the studied basalts. This observation aligns with research on other volcanic systems, such as the Hawaiian shield stage lavas, where the crystallization of clinopyroxene and garnet has been linked to melts rich in SiO_2. These SiO_2-rich melts are believed to originate from a pyroxenite source and occur at high pressures, approximately $\sim$ 4 GPa (Herzberg, 2011). High-pressure experiments have further contributed to our understanding of the processes involved. These experiments have demonstrated that the initial depth of melting for garnet pyroxenitic rocks is relatively shallow, occurring at depths of less than 100 km (Kogiso et al.,
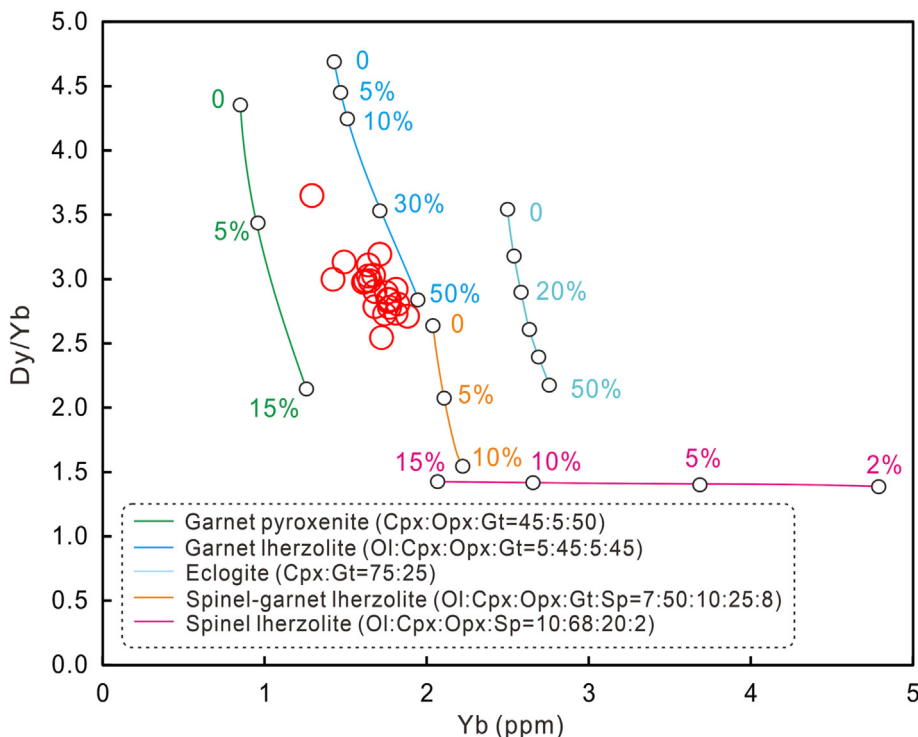
Fig. 12. Plot of Dy/Yb ratio versus Yb (after An et al., 2017; Yan et al., 2018). Abbreviations: Ol = olivine; Opx = orthopyroxene; Cpx = clinopyroxene; Sp = spinel; and Gt = garnet.

2003). Based on this information, we propose that the UMVC can be attributed to the presence of both garnet pyroxenite melts and garnet lherzolite melts.

To determine the original depth and pressure associated with the studied basalts, we applied the standard CIPW algorithm. Our results indicate that the original depth and pressure ranges linked to the formation of rocks in the UMVC are ∼ 70–100 km and ∼ 2–3 GPa, respectively (Fig. S6). These findings are consistent with experimental data on clinopyroxene and garnet stability at depths of approximately 70–100 km (Green and Ringwood, 1967). Although a thick lithosphere (∼120–200 km; Fig. 1b) exists beneath the TNCO–WB, a thinned lithosphere (∼80 km) has been reported in the Late Cenozoic Yinchuan–Hetao and Shaanxi–Shanxi rift areas near Ulanqab (Zhang et al., 2012). This observation underscores the dynamic nature of lithospheric thickness in the region. Additionally, the high Nb/La ratios (1.03–1.63) of the UMVC samples are comparable to those of an asthenospheric mantle source (>1; Smith et al., 1999). The Ulanqab basalts (120–109 Ma), excluding UMVC, are associated with a metasomatized (enriched) lithospheric mantle origin. These basalts are characterized by high ($^{87}Sr/^{86}Sr$)$_i$ and low ε_{Nd}(t) values. Conversely, Quaternary basalts in the Ulanqab basalts of asthenospheric origin exhibit low ($^{87}Sr/^{86}Sr$)$_i$ and high ε_{Nd}(t) values (Fig. 10b; Guo et al., 2014). These data represent further evidence of lithospheric thinning beneath the WB during Late Cretaceous to Quaternary. Spatial and temporal variations of the lithosphere in the Tianheyong (western Ulanqab) and Hannuoba (eastern Ulanqab) areas during the Miocene indicate intense thermal erosion of the metasomatized lithosphere by the upwelling asthenosphere (Song et al., 1990; Tang et al., 2007). The transition from the lithospheric to asthenospheric mantle was examined in a study by Humphreys and Niu (2009), revealing that this transition occurred during decompression, indicating significant changes in the mantle's structure and composition. Another study by Kiseeva et al. (2018) discovered that garnet plays a stabilizing role in the mantle

transition zone (MTZ) and can exist on the solidus of pyroxenite even at lower pressures (Hirschmann and Stolper, 1996). These findings suggest that garnet and clinopyroxene likely act as residual phases in the asthenospheric mantle near the lithosphere-asthenosphere boundary (LAB). This raises the possibility of silica-rich garnet pyroxenite stagnating in this region, which can serve as a potential source for alkali basalts. As a result, the LAB emerges as a prime location for mantle metasomatism associated with OIB source (Wilson and Downes, 1991).

Moreover, the presence of subducted carbonates is strongly indicated by several lines of evidence. Carbonates are known to exhibit significantly lower $\delta^{26}Mg$ values (−4.84 to − 1.09) compared to other reservoirs (Young and Galy, 2004; Geske et al., 2015), providing a foundational basis for our interpretation of the light Mg isotope composition (−0.56 ‰ to − 0.42 ‰) observed in UMVC rocks. Moreover, the UMVC samples exhibit distinct elemental patterns, showing enrichment in Ba but depletion in Zr, Hf, and Ti—characteristic of carbonates (Hoernle et al., 2002; Bizimis et al., 2003). These geochemical patterns find further support in the low Ti/Ti* and Hf/Hf* ratios, regarded as "carbonatitic fingerprints" (Zeng et al., 2010). Notably, our UMVC samples display low Ti/Ti* (0.71–0.87) and Hf/Hf* (0.72–0.95) ratios, aligning with the observed low trend $\delta^{26}Mg$ basalts from the NCC (Fig. S7). To further strengthen our understanding of mantle origin and its connection to carbonates, it's essential to consider the behavior of clinopyroxene. Clinopyroxene, an early-stage mineral of carbonated silicate melts, commonly crystallizes from magmas containing high Ca, such as carbonated melts. This observation provides significant insights into the origin of the mantle (Fig. S1b; Beccaluva et al., 1992; Ivanikov et al., 1998). It is imperative to note that carbonatitic melts undergo a transformation into carbonated silicate melts, a process that intensifies with augmented temperature and enhanced degrees of melt extraction. This evolution arises from the pronounced dissolution of clinopyroxene and/or olivine into the carbonatitic melts, thereby amplifying the melt fraction

and concurrently diluting the concentration of carbon dioxide (CO_2) within the melts (Dasgupta, 2013). Therefore, it is likely that carbonated silicate melts contributed to the formation of melts from which the UMVC originated.

In subducting slabs, stable Mg-rich carbonate minerals (dolomite and magnesite) may be present due to interactions between silicates and carbonates (Wang and Li, 2022). Variations in the $\delta^{26}Mg$ and MgO data in the samples from the UMVC can be modeled by a mixing of mid-ocean ridge basalt with Mg-rich carbonate melts (Fig. S4a). These findings suggest that approximately 15 %–20 % of the UMVC's mantle source contained Mg-rich carbonates. Additionally, since there is limited Mg and Sr isotope fractionation during basalt differentiation (Teng et al., 2007), the isotope ratios of these elements in basalts can provide insights into carbonates in the pyroxenitic mantle. This points to a hybrid source that has undergone carbonate metasomatism, supported by a positive correlation with "carbonatitic fingerprints" anomalies (Fig. S7; Yang et al., 2012). Our study supports the hypothesis that the observed Mg–Sr isotope mixing models can be attributed to the intricate mixing of varying quantities and proportions of dolomite and magnesite within the mantle sources of UMVC magmas (Fig. 13). Our findings reveal mantle heterogeneity, a result of the variable presence of subducted carbonates within the mantle. This mantle heterogeneity is a consequence of the uneven input of carbonates during magma upwelling—a dynamic process that fundamentally shapes the geological history of our study region. Importantly, these implications extend beyond the UMVC, reaching the broader context of Cenozoic basalts across the EB. The isotopic ratios reported for these basalts align consistently with the explanation grounded in carbonate mixing and mantle heterogeneity (Wang et al., 2016; Xu et al., 2018). In conclusion, the compositional variations of alkaline basalts from eastern China reflect different proportions of diverse carbonate components in their mantle sources. This underscores the clear influence of mantle heterogeneity on volcanic activity, even under identical or similar tectonic conditions.
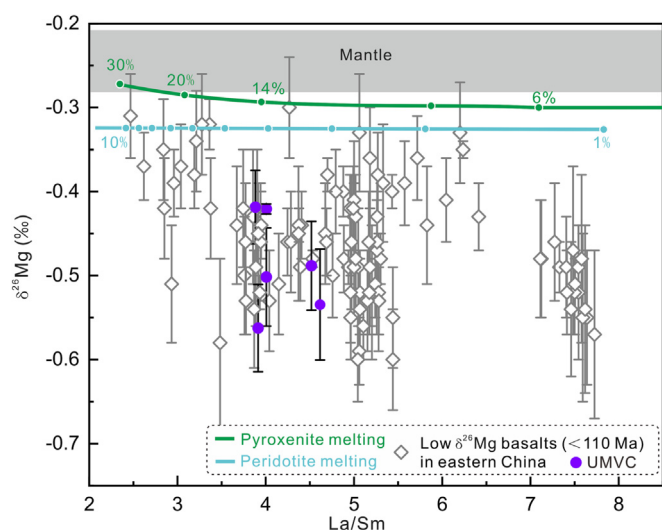

Fig. 13. Plot of $\delta^{26}Mg$ versus $^{87}Sr/^{86}Sr$ exhibit a mixing model between peridotitic mantle and subducted carbonates. Points on mixing curves are at 5 % intervals. The label on each curve is the proportion of dolomite: magnesite. The peridotitic mantle and isotopic compositions are citied from Teng (2017) and He et al. (2019), respectively. The Fuxin (106–100 Ma), Taihang (26–6 Ma), Hannuoba (22–14 Ma), Wulanhada (0.36–0.22 Ma), and Changbaishan (2.8–0.3 Ma) Cenozoic basalts for Mg-Sr isotopic data of NCC are from Li et al. (2017), Yang et al. (2012), Tian et al. (2019), and Sun et al. (2021).

5.2. Crystallization and differentiation of the basaltic magma

Variable Ni contents (487–2239 ppm) in olivine phenocrysts from the UMVC indicate that these rocks underwent certain magmatic evolution and did not reach equilibrium with primary mantle olivine (Langmuir et al., 1977; Aldanmaz et al., 2006). The Ni data for the samples exhibit a negative correlation with SiO_2 (Fig. S8a), suggesting that fractional crystallization likely played a role in the evolution of the parental magmas of the UMVC. Additionally, positive correlations between Ni and Cr, as well as between CaO/Al_2O_3 and CaO (Fig. S8b and c), indicate fractional crystallization of olivine and clinopyroxene. In contrast, the slightly negative Ti anomalies (Fig. 9b) and the lack of correlation between TiO_2 and the Mg# (Fig. S8d) exclude significant fractional crystallization of ilmenite.

The acquisition of alkalinity in magmas is a significant factor to consider, as it plays a crucial role in the formation of alkaline basalts, and it is believed to involves magma evolution processes occurring at greater depths than those of oceanic tholeiites (Green et al., 1967; Tatsumi et al., 1983). Processes such as segregation or fractional crystallization contribute to the enrichment of alkaline components in the magmas. In the case of already alkaline magmas, a typical narrative of evolution is observed. Basaltic magmas tend to accumulate in chambers and, as they cool, a crystal mush is formed in the shallow lithosphere (Cooper and Kent, 2014). Within this crystal mush, mantle-derived magmas can be injected, causing the fragmented crystals to undergo disaggregation. These fragmented crystals are then transported within the magma to the surface, resulting in the formation of glomerocrysts (Pan et al., 2022).

The UMVC samples exhibit negative Rb anomalies, high concentrations of Ba (337–744 ppm), and moderate to high concentrations of Sr (557–1230 ppm). Negligible negative Eu anomalies (Eu/Eu* = 0.93–1.08) ratios are also observed, along with a gregarious texture (Figs. 5 and S9). These features strongly suggest that the formation of these alkali basalts is closely associated with the accumulation of crystals within the magma chamber.

To gain further insights into the crystallization process, a simulation of the crystalline phase equilibrium of the UMVC samples was performed using the Rhyolite-MELTS software (version 1.2.0; Gualda et al., 2012). The simulation, based on an initial pressure of 0.3 GPa, used the composition of sample HZ21 as representative of the initial melt and assumed an initial magma water content of 0.5 wt% (cf. Whitaker et al., 2007). The results of the simulation (Fig. S10) indicate that magma crystallization commenced at approximately 1250 °C. The earliest stage of this crystallization involved the gradual increase in the proportion of olivine, followed by the development of pyroxenes and feldspars. Moreover, the data for the UMVC samples fall within the field of liquid + olivine + plagioclase + augite cotectic at low pressure (<0.4 GPa), indicating that the evolved clinopyroxene and olivine samples experienced fractional crystallization in the shallow part of the lithosphere (Fig. 14). These findings are corroborated by normative mineral calculations (Fig. S11) and photomicrographs illustrating the crystallized minerals (Fig. 5).

5.3. Geodynamic controls on magmatic processes

Alkaline lavas often exhibit chemical variations primarily controlled by simple mixing of end-members (Weinstein et al., 2006). Melt mixing, on the other hand, is typically associated with mantle plumes or conducting mantle melts (Li et al., 2003). In the case of the UMVC, the question arises whether the alkalinity of the magmas was acquired through mantle plume activity. One characteristic of a mantle plume would be higher heat flow in the Northeastern WB, leading to regional uplift and the formation of dome
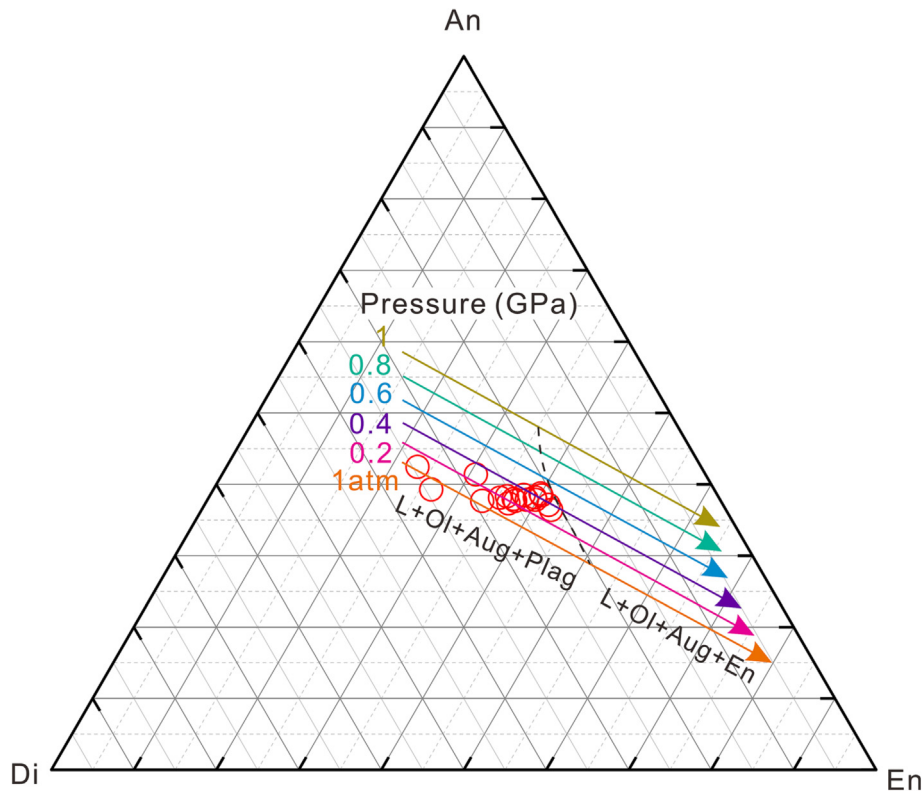
Fig. 14. Triangular diagram of Anorthite (An)–Diopside (Di)–Enstatite (En) for an anhydrous system (Herzberg, 2004). All weight per cent compositions were converted to mole per cent. The arrow indicates decreasing temperature. Abbreviations: Aug = augite; L = liquid; Plag = plagioclase.

structures due to maximum extensional stress (Hansen et al., 2000). However, surface heat flow values reported for the study area are low, suggesting the absence of a plume feature (Zheng et al., 2021). Additionally, variations in depth from the garnet to spinel facies mantle and changes in the degree of partial melting, typically associated with a mantle plume, are not reflected in the study area. This suggests that upwelling in the UMVC region was likely triggered by an upper mantle melt anomaly dominated by late-stage extension, possibly representing a compositional anomaly zone in the shallow convective mantle (Aldanmaz et al., 2006). Therefore, while mantle plumes are commonly associated with the formation of alkaline lavas through melt mixing, the specific geodynamic controls in the UMVC region appear to be different. The alkalinity of the magmas in this area is more likely attributed to an upper mantle melt anomaly related to late-stage extension and a compositional anomaly zone within the shallow convective mantle.

The UMVC samples exhibit low δ^{26}Mg values (−0.56 ‰ to − 0.42 ‰), as well as lower Ba/Rb (15.60–41.63) and CaO/Al$_2$O$_3$ ratios (0.49–0.72), similar to those observed in Cenozoic basalts from eastern China (Fig. 3b and S12; Li et al., 2017; Su et al., 2017; Sun et al., 2021). This similarity suggests a connection between the UMVC and a carbon reservoir. The presence of this reservoir has been confirmed in the overlying convection-related upper mantle beneath eastern China since the Mesozoic Pacific Plate subduction, at depths of approximately 410–660 km (Liu et al., 2022). It is a commonly proposed explanation for the low Mg isotope compositions of Cenozoic OIB-like basalts in eastern China (Fig. 9; Yang et al., 2012). In other words, it suggests that the EB probably experienced carbonate metasomatism linked to the PPO (Izanagi) slab in the Mesozoic–Cenozoic or Pacific slab subduction during the Cenozoic (Maruyama et al., 1997; Liu et al., 2020). This process led to the incorporation of low Mg iso-

tope signatures in rocks from Cenozoic intraplate volcanoes (Su et al., 2017). Nonetheless, seismic imaging of the northwest Pacific does not reveal a stagnant slab (Pacific slab) in the WB (Zhao, 2021). The Sr–Nd isotope compositions of the UMVC samples provide evidence of contributions originating from an EM1-like mantle source. However, these compositions diverge from those found in Cenozoic basalts in eastern China (Fig. 10). Additionally, high Ba/Th ratios (123–215) and low TFeO concentrations (9.95–11.68) in the studied samples further indicate that the enriched components likely originated from ancient marine sedimentary carbonate (Fig. S13; Li et al., 2014). Therefore, this source likely has its origins in carbonate-bearing sediments associated with a subduction event distinct from that which involves the Pacific Plate (Sun et al., 2021; Tian et al., 2016; Wang et al., 2017).

The origin of subducted sedimentary carbonate in geological processes is a complex matter. It is essential to investigate where this material comes from and how it interacts within the mantle. It's crucial to note that the absence of a stagnant slab directly beneath the WB volcanic field, as revealed by seismic tomography, does not necessarily imply its historical non-existence. The low CaO/Al$_2$O$_3$ ratios (0.49–0.72) and presence of "carbonatitic fingerprints" also suggests the UMVC' magmas derived from ancient subducted slabs (Figs. S7 and S11; Chen et al., 2022).

Numerous investigations have postulated the potential of the MTZ to function as a reservoir for retaining subducted sediments over protracted intervals, thereby possibly giving rise to the formation of an EM1 reservoir (e.g., Li et al., 2020; Rapp et al., 2008; Wang et al., 2017). Subducted carbonate-bearing sediments, in conjunction with a Precambrian subducted slab, undergo complex geological processes as they traverse the mantle and encounter the MTZ. In this transitional zone, these sediments encountered high pressures and temperatures, leading to their deflection along the 660 km discontinuity. This process induced partial melting of the

sediments, culminating in the genesis of carbonate melts (Fig. 15a). This implies that the local MTZ represents an exceptionally suitable repository for harboring ancient subducted sediments. As the stagnant slab gradually undergoes thermal modification, the process of decarbonation melting of subducted sedimentary components is likely situated within the confines of the MTZ (Zeng et al., 2021; Fig. 15a). Notably, numerical simulations suggest that decarbonation at Precambrian subduction zones occurred at higher temperatures (up to ∼ 100℃) than in present-day subduction zones (Sizova et al., 2010). However, factors such as the degree of partial melting in deep mantle sources, as well as prevailing pressure and temperature conditions, may exert an influence on the correlation between low Mg isotope values and the decarbonation process.

The $\delta^{26}Mg$ values in our basalts exhibit a negative correlation with the quantities of incompatible elements and the abundance ratios of trace elements sensitive to partial melting (Fig. S14). This observation implies relative fluctuations in Mg isotope ratios during the process of mantle partial melting, transpiring under conditions of elevated temperatures and pressures. Concurrently, associated research corroborates an increase in Ti/Ti* ratios and a decrease in Zr/Hf ratios as basalts undergo greater degrees of partial melting (Huang et al., 2015). At higher degrees of partial melting, the predominant contributors are isotopically heavy carbonated silicate melts, typified by reduced Zr/Hf ratios and augmented Ti/Ti* ratios (Figs. S7 and S15). Consequently, the low Mg isotopic compositions within our basalts epitomize the metasomatism by carbonated silicate melts, as opposed to isotopic fractionation transpiring within mantle conditions of temperature and pressure. To contextualize these findings, it is essential to consider the geological history of the lithospheric mantle in Eastern China.

The lithospheric mantle in Eastern China, including Ulanqab, primarily formed between the Early and Middle Proterozoic (Xia et al., 2004). Its coherence with the Nd ages (1.02–1.51 Ga) of the studied basaltic rocks substantiates the notion that the mantle lithosphere influenced by Cenozoic thinning is a remnant of the mid-Proterozoic lithosphere. Moreover, the UMVC samples exhibit low Nb/Th ratios ranging from 8.07 to 15.20, pointing toward an ancient source of pelagic carbonate. Remarkably, this source exhibits similarities to the Pitcairn EM1 basalts (Wang et al., 2018). These components, such as garnet pyroxenite (Sobolev et al., 2007), are attributed to the Indian Mantle and possibly linked to the thermo-mechanical erosion of the ancient lithospheric mantle by the conductive mantle (Xu et al., 2018). It appears that these signatures are more likely associated with carbonates undergoing early decarbonation during subduction, rather than carbonate components being subducted into the lower mantle. It is worth noting that there is a conspicuous absence of residual carbonate minerals within these samples. This seeming paradox can be elucidated by contemplating the possibility that the UMVC samples might indeed signify the formation of decarbonated residues during the subduction process. Carbonatite melts, when subjected to subduction processes, undergo substantial decarbonation. This results in a significant reduction in their carbonate content, leaving behind only a meager residue. Such carbonate-depleted residues would inherit the characteristic light Mg isotopic signature from their parent protolith (Macris et al., 2013). One aspect to consider is how these Mg isotope fingerprints of carbonates are retained or transferred during the decarbonation process. Recent research by Wang and Li (2022) suggests that newly formed silicates can effectively preserve the Mg isotope compositions of carbonates during decarbonation. Alternatively, the light Mg isotope composition of carbonates can be transferred to silicates via decarbonation processes (Wang et al., 2014). In conclusion, the absence of residual carbonate minerals in UMVC samples can be explained by the decarbonation process, leading to the formation of carbonate-depleted residues with distinct Mg isotopic signatures. The retention and transfer of these isotopic fingerprints in newly formed silicates unravel the intricate geochemical processes occurring during subduction.

Building upon our understanding of the intricate geochemical processes occurring during subduction, we now propose a comprehensive multistep genetic model for alkaline basalts, drawing upon the results of our integrated study. The model unfolds as follows: Subducted carbonates play a crucial role in early decarbonation in the MTZ, resulting in relatively low $\delta^{26}Mg$ values in residual
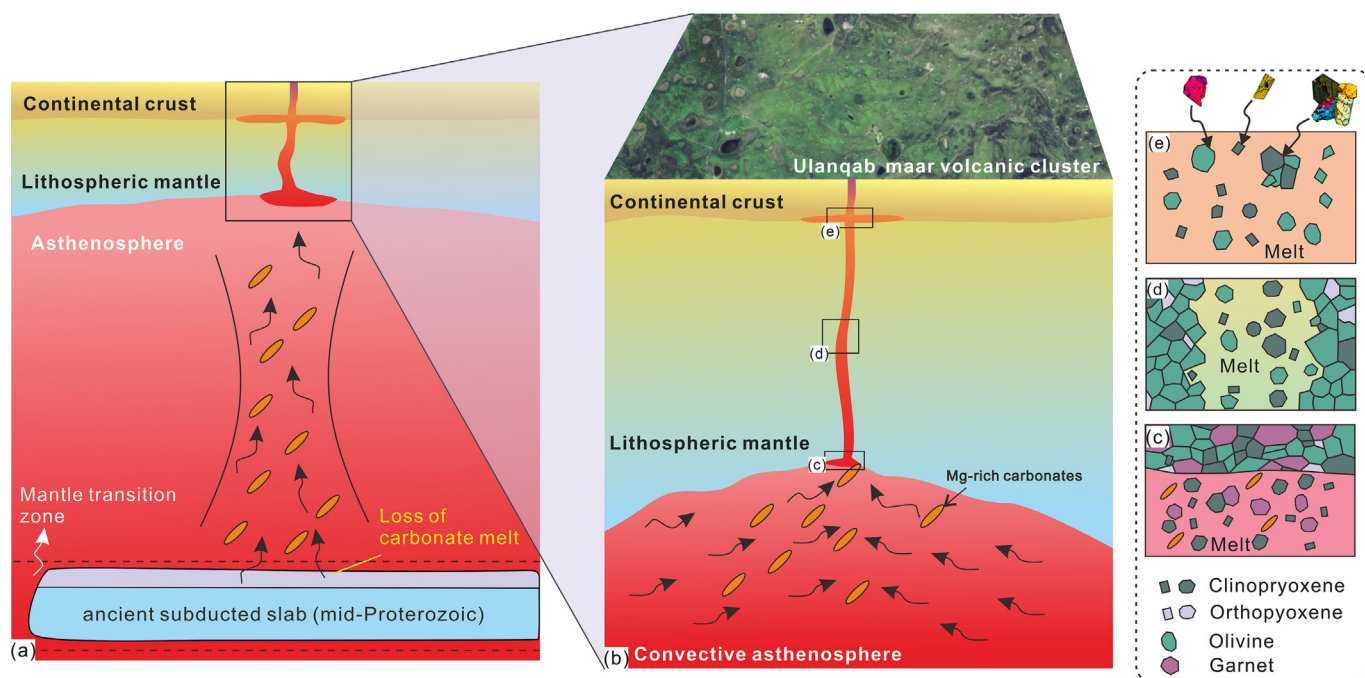

Fig. 15. Schematic diagrams showing the magmatic processes throughout in the deep to shallow magma reservoir. Detailed explanations are in the text.

pyroxenite (Fig. 15a). This process becomes particularly significant in cases where the lithosphere is thin (<80 km) during the Late Cenozoic. The upwelling asthenosphere acts as a conduit for metasomatized materials from the base of the ancient oceanic lithosphere, triggering the crystallization of magma. Within the deep magma chamber at the LAB, the fractional crystallization of clinopyroxene (Cpx) and garnet from the primitive magma produces high-Ti alkaline lavas (Fig. 15b). Although clinopyroxene and garnet are early-stage crystalline minerals, their primary crystallization predominantly occurs within the depths of magma chambers. This can be attributed to the sluggish ascent rate of magma in the profound lithospheric mantle, which hampers its ability to efficiently transport significant quantities of clinopyroxene and garnet. Even when a small amount of clinopyroxene and garnet is entrained in the magma, their interaction with silica-undersaturated magma during the ascent process results in their near virtual absence within the ejected lavas. In contrast, within the shallower lithospheric mantle, a remarkable phenomenon unfolds. The intricate interplay between melt and orthopyroxenite engenders a profound surge in the rate of magma migration (Daines and Kohlstedt, 1994). In this regard, alkaline magma percolates through the LAB and interacts with orthopyroxene (Opx) under low-pressure conditions. The ensuing reaction, depicted in Fig. 15c as Opx + Melt (silica poor) = Olivine + Melt (silica rich) + Cpx, engenders a momentous augmentation in the magma's transport kinetics. Consequently, it enhances the crystallization of olivine and clinopyroxene in the shallow lithosphere (Fig. 15d).

Therefore, the statement suggests that the interaction between alkaline magma and orthopyroxenite in the shallow lithospheric mantle facilitates the formation and crystallization of olivine and clinopyroxene, contributing to the overall volcanic activity in this region.

6. Conclusions

In the present study, plagioclase samples yielded an $^{40}Ar/^{39}Ar$ age of 7.60 ± 0.04 Ma for the UMVC. This age marked the eruptions that produced the associated alkaline basalts, and thus, these were younger than Hannuoba basalts but older than Quaternary basalts.

According to our new data the UMVC was associated with an enriched mantle source (EMI-like) that was possibly linked to garnet pyroxenitic and garnet lherzolitic source. The light Mg isotope composition exhibited by the samples studied was attributed to a carbonate metasomatized hybrid source associated with early decarbonation at Precambrian subduction zones. Thus, Mg-rich carbonate minerals (magnesite ± dolomite) in marine sediments were incorporated into the magma source. The variations we see in the alkaline basalts in eastern China are because they come from different combinations of carbonate materials deep within their mantle sources.

Crystallization of clinopyroxene and garnet occurs within the deep magma chamber, resulting in the formation of high-Ti alkaline lavas. However, the sluggish ascent rate of magma in the profound lithospheric mantle limits the transport of clinopyroxene and garnet, leading to their near absence in the erupted lavas. In contrast, in the shallower lithospheric mantle, the interaction between alkaline magma and orthopyroxenite enhances magma transport kinetics. This interaction promotes the crystallization of clinopyroxene and olivine occurred under lower-pressure conditions. These magmas involved mafic residual crystal mushes from accumulation chambers.

Convecting asthenospheric mantle upwelling beneath the WB through the LAB produced an extensional setting, and this contributed to the formation of the UMVC. The OIB-like basalt melts were derived from the interaction of melts of the underlying con-

vecting asthenospheric mantle and those of the sub-continental mantle related to ancient subduction. The formation of the UMVC is likely unrelated to the subducting Pacific or PPO slab but is instead closely linked to an earlier subduction event that involved carbonate metasomatism.

CRediT authorship contribution statement

Zong-yuan Tang: Methodology, Writing – original draft. **Chen-chang Chen:** Visualization, Writing – review & editing. **Si-ying Gui:** Methodology, Investigation, Visualization. **Jie Li:** Software, Validation. **De-you Sun:** Data curation. **Chang-zhou Deng:** Investigation, Data curation. **Han Zheng:** Methodology. **Guo-chun Zhao:** Supervision, Conceptualization, Funding acquisition.

Declaration of competing interest

The authors declare that they have no known competing financial interests or personal relationships that could have appeared to influence the work reported in this paper.

Acknowledgments

Appendix A. Supplementary data

Supplementary data to this article can be found online at https://doi.org/10.1016/j.gr.2023.10.011.

References

Aldanmaz, E.R.C.A.N., Köprübaşı, N., Gürer, Ö.F., Kaymakcı, N., Gourgaud, A., 2006. Geochemical constraints on the Cenozoic, OIB–type alkaline volcanic rocks of NW Turkey: implications for mantle sources and melting processes. Lithos 86 (1–2), 50–76.

An, A.R., Choi, S.H., Yu, Y., Lee, D.C., 2017. Petrogenesis of Late Cenozoic basaltic rocks from southern Vietnam. Lithos 272, 192–204.

An, Y., Wu, F., Xiang, Y., Nan, X., Yu, X., Yang, J., Yu, H., Xie, L., Huang, F., 2014. High–precision Mg isotope analyses of low–Mg rocks by MC-ICP–MS. Chem. Geol. 390, 9–21.

Beccaluva, L., Barbieri, M., Born, H., Brotzu, P., Coltorti, M., Conte, A., Garbarino, C., G. C.B.G, M.A., Morbidelli, L., Ruberti, E., Siena, F., Traversa, G., 1992. Fractional crystallization and liquid immiscibility processes in the alkaline-carbonatite complex of Juquiá (São Paulo, Brazil). J. Petrol. 33(6), 1371–1404.

Blichert-Toft, J., Albarede, F., Kornprobst, J., 1999. Lu–Hf isotope systematics of garnet pyroxenites from Beni Bousera, Morocco: implications for basalt origin. Science 283 (5406), 1303–1306.

Boynton, W.V., 1984. Cosmochemistry of the Rare Earth Elements: Meteorite Studies. In: Henderson, P. (Ed.), Rare Earth Element Geochemistry. Elsevier, Amsterdam, pp. 63–114.

Chen, L., Cheng, C., Wei, Z., 2009. Seismic evidence for significant lateral variations in lithospheric thickness beneath the central and western North China Craton. Earth Planet Sc. Lett. 286 (1–2), 171–183.

Chen, L.H., Wang, X.J., Liu, S.A., 2022. Probing recycled carbonate in the lower mantle. Natl. Sci. Rev. 9 (6), nwac061.

Chen, Y., Zhang, Y., Graham, D., Su, S., Deng, J., 2007. Geochemistry of Cenozoic basalts and mantle xenoliths in Northeast China. Lithos 96 (1–2), 108–126.

Cooper, K.M., Kent, A.J., 2014. Rapid remobilization of magmatic crystals kept in cold storage. Nature 506 (7489), 480–483.

Dai, L.Q., Zhao, Z.F., Zheng, Y.F., An, Y.J., Zheng, F., 2017. Geochemical distinction between carbonate and silicate metasomatism in generating the mantle sources of alkali basalts. J. Petrol. 58 (5), 863–884.

Daines, M.J., Kohlstedt, D.L., 1994. The transition from porous to channelized flow due to melt/rock reaction during melt migration. Geophys Res. Lett. 21 (2), 145–148.

Dasgupta, R., 2013. Ingassing, storage, and outgassing of terrestrial carbon through geologic time. Rev. Mineral. Geochem. 75 (1), 183–229.

Dasgupta, R., Hirschmann, M.M., Stalker, K., 2006. Immiscible transition from carbonate-rich to silicate-rich melts in the 3 GPa melting interval of eclogite+ CO_2 and genesis of silica-undersaturated ocean island lavas. J. Petrol. 47 (4), 647–671.

Dasgupta, R., Hirschmann, M.M., Smith, N.D., 2007. Partial melting experiments of peridotite + CO_2 at 3 GPa and genesis of alkalic ocean island basalts. J. Petrol. 48, 2093–2124.

Dong, J., Song, S., Su, L., Li, Y., Yang, L., Wang, C., Xu, B., 2019. Onset of the North-South Gravity Lineament, NE China: constraints of late Jurassic bimodal volcanic rocks. Lithos 334, 58–68.

Fan, Q.C., Chen, S.S., Zhao, Y.W., Zou, H.B., Li, N., Sui, J.L., 2014. Petrogenesis and evolution of Quaternary basaltic rocks from the Wulanhada area, North China. Lithos 206, 289–302.

Geske, A., Goldstein, R.H., Mavromatis, V., Richter, D.K., Buhl, D., Kluge, T., John, C.M., Immenhauser, A., 2015. The magnesium isotope ($\delta 26Mg$) signature of dolomites. Geochim. Cosmochim. Acta 149, 131–151.

Gómez-Ulla, A., Sigmarsson, O., Huertas, M.J., Devidal, J.L., Ancochea, E., 2018. The historical basanite-alkali basalt-tholeiite suite at Lanzarote, Canary Islands: Carbonated melts of heterogeneous mantle source? Chem. Geol. 494, 56–68.

Graettinger, A.H., 2018. Trends in maar crater size and shape using the global Maar Volcano Location and Shape (MaarVLS) database.J. Volcanol. Geoth. Res. 357, 1–13.

Green, T.H., Green, D.H., Ringwood, A.E., 1967. The origin of high-alumina basalts and their relationships to quartz tholeiites and alkali basalts. Earth Planet Sc. Lett. 2 (1), 41–51.

Green, D.H., Ringwood, A.E., 1967. The genesis of basaltic magmas. Contrib. Mineral. Petr. 15 (2), 103–190.

Gualda, G.A., Ghiorso, M.S., Lemons, R.V., Carley, T.L., 2012. Rhyolite-MELTS: a modified calibration of MELTS optimized for silica-rich, fluid-bearing magmatic systems. J. Petrol. 53 (5), 875–890.

Guo, P., Niu, Y., Ye, L., Liu, J., Sun, P., Cui, H., Zhang, Y., Gao, J., Su, L., Zhao, J., Feng, Y., 2014. Lithosphere thinning beneath west North China Craton: evidence from geochemical and Sr–Nd–Hf isotope compositions of Jining basalts. Lithos 202, 37–54.

Guo, P., Niu, Y., Sun, P., Gong, H., Wang, X., 2020. Lithosphere thickness controls continental basalt compositions: An illustration using Cenozoic basalts from eastern China. Geology 48 (2), 128–133.

Hansen, V.L., Phillips, R.J., Willis, J.J., Ghent, R.R., 2000. Structures in tessera terrain, Venus: Issues and answers. J. Geophys. Res.: Planets 105 (E2), 4135–4152.

He, Y., Chen, L.H., Shi, J.H., Zeng, G., Wang, X.J., Xue, X.Q., Zhong, Y., Erdmann, S., Xie, L.W., 2019. Light Mg isotopic composition in the mantle beyond the Big Mantle Wedge beneath eastern Asia. J. Geophys. Res.: Solid. Earth 124 (8), 8043–8056.

Herzberg, C., 2004. Partial crystallization of mid–ocean ridge basalts in the crust and mantle. J. Petrol. 45 (12), 2389–2405.

Herzberg, C., 2011. Identification of source lithology in the Hawaiian and Canary Islands: Implications for origins. J. Petrol. 52 (1), 113–146.

Hirschmann, M.M., Stolper, E.M., 1996. A possible role for garnet pyroxenite in the origin of the garnet signature‖ in MORB. Contrib. Mineral. Petrol. 124, 185–208.

Hofmann, A.W., 1997. Mantle geochemistry: the message from oceanic volcanism. Nature 385 (6613), 219–229.

Huang, S., Frey, F.A., 2005. Recycled oceanic crust in the Hawaiian Plume: evidence from temporal geochemical variations within the Koolau Shield. Contrib. Mineral. Petrol. 149, 556–575.

Huang, J., Li, S.G., Xiao, Y., Ke, S., Li, W.Y., Tian, Y., 2015. Origin of low $\delta^{26}Mg$ Cenozoic basalts from South China Block and their geodynamic implications. Geochim. Cosmochim. Ac. 164, 298–317.

Huang, S., Zheng, Y., 2017. Mantle geochemistry: Insights from ocean island basalts. Sci. China Earth Sci. 60 (11), 1976–2000.

Humphreys, E.R., Niu, Y., 2009. On the composition of ocean island basalts (OIB): The effects of lithospheric thickness variation and mantle metasomatism. Lithos 112 (1–2), 118–136.

Irvine, T.H., Baragar, W.R.A., 1971. A Guide to the Chemical Classification of the Common Volcanic Rocks. Can. J. Earth Sci. 8, 523–548.

Ivanikov, V.V., Rukhlov, A.S., Bell, K., 1998. Magmatic evolution of the melilitite-carbonatite-nephelinite dyke series of the Turiy Peninsula (Kandalaksha Bay, White Sea, Russia). J. Petrol. 39 (11–12), 2043–2059.

Kiseeva, E.S., Vasiukov, D.M., Wood, B.J., McCammon, C., Stachel, T., Bykov, M., Bykova, E., Chumakov, A., Cerantola, V., Harris, J.W., Dubrovinsky, L., 2018. Oxidized iron in garnets from the mantle transition zone. Nat. Geosci. 11 (2), 144–147.

Kogiso, T., Hirschmann, M.M., Frost, D.J., 2003. High–pressure partial melting of garnet pyroxenite: possible mafic lithologies in the source of ocean island basalts. Earth Planet Sc. Lett. 216 (4), 603–617.

Kogiso, T., Hirschmann, M.M., 2006. Partial melting experiments of bimineralic eclogite and the role of recycled mafic oceanic crust in the genesis of ocean island basalts. Earth Planet. Sci. Lett. 249 (3–4), 188–199.

Langmuir, C.H., Bender, J.F., Bence, A.E., Hanson, G.N., Taylor, S.R., 1977. Petrogenesis of basalts from the FAMOUS area: Mid-Atlantic Ridge. Earth Planet Sc. Lett. 36 (1), 133–156.

Li, H.Y., Huang, X.L., Guo, H., 2014. Geochemistry of Cenozoic basalts from the Bohai Bay Basin: Implications for a heterogeneous mantle source and lithospheric evolution beneath the eastern North China Craton. Lithos 196, 54–66.

Li, Y.Q., Kitagawa, H., Nakamura, E., Ma, C., Hu, X., Kobayashi, K., Sakaguchi, C., 2020. Various ages of recycled material in the source of Cenozoic basalts in SE China: Implications for the role of the Hainan Plume. J. Petrol. 61 (6), egaa060.

Li, X.H., Li, Z.X., Ge, W., Zhou, H., Li, W., Liu, Y., Wingate, M.T., 2003. Neoproterozoic granitoids in South China: crustal melting above a mantle plume at ca. 825 Ma? Precambrian Res. 122 (1–4), 45–83.

Li, S.G., Yang, W., Ke, S., Meng, X., Tian, H., Xu, L., He, Y., Huang, J., Wang, X.C., Sun, W., Yang, X., Ren, Z.Y., Wei, H., Liu, Y., Meng, F., Yan, J., 2017. Deep carbon cycles constrained by a large–scale mantle Mg isotope anomaly in eastern China. Natl. Sci. Rev. 4 (1), 111–120.

Liu, J., 1999. Volcanoes in China. Science Press, Beijing, p. 219 (in Chinese).

Liu, R., Chen, W., Sun, J., Li, D., 1992b. K-Ar age and tectonic environment of Cenozoic volcanic rock in China. In: Liu, R. (Ed.), Age and Geochemistry of Cenozoic Volcanic Rock in China. Seismology Published House, Beijing, pp. 1–43 (in Chinese).

Liu, S.A., Li, S.G., 2019. Tracing the deep carbon cycle using metal stable isotopes: opportunities and challenges. Engineering 5 (3), 448–457.

Liu, D.Y., Nutman, A.P., Compston, W., Wu, J.S., Shen, Q.H., 1992a. Remnants of≥ 3800 Ma crust in the Chinese part of the Sino-Korean craton. Geology 20 (4), 339–342.

Liu, S.A., Qu, Y.R., Wang, Z.Z., Li, M.L., Yang, C., Li, S.G., 2022. The fate of subducting carbon tracked by Mg and Zn isotopes: A review and new perspectives. Earth-Sci. Rev. 228, 104010.

Liu, K., Zhang, J., Xiao, W., Wilde, S.A., Alexandrov, I., 2020. A review of magmatism and deformation history along the NE Asian margin from ca. 95 to 30 Ma: Transition from the Izanagi to Pacific plate subduction in the early Cenozoic. Earth-Sci. Rev. 209, 103317.

Ma, L., Jiang, S., Hofmann, A.W., Dai, B., Hou, M., Zhao, K., Chen, L., Li, J., Jiang, Y., 2014. Lithospheric and asthenospheric sources of lamprophyres in the Jiaodong Peninsula: a consequence of rapid lithospheric thinning beneath the North China Craton? Geochim. Cosmochim. Acta 124, 250–271.

Macris, C.A., Young, E.D., Manning, C.E., 2013. Experimental determination of equilibrium magnesium isotope fractionation between spinel, forsterite, and magnesite from 600 to 800∘C. Geochim. Cosmochim. Acta 118, 18–32.

Maruyama, S., Isozaki, Y., Kimura, G., Terabayashi, M., 1997. Paleogeographic maps of the Japanese Islands: Plate tectonic synthesis from 750 Ma to the present. Isl. Arc 6 (1), 121–142.

Mondal, N.N., Debnath, T.K., Roy, T.K., Saha, K.D., Alam, B., Sarkar, M., Hennrich, F., Mommsen, H., Lui, A., 1994. Determination of arsenic content in the waste sludge from a fertilizer factory of Bangladesh by XRF and EPMA. Appl. Radiat. Isot. 45 (9), 945–948.

Nesbitt, H., Young, G.M., 1982. Early Proterozoic climates and plate motions inferred from major element chemistry of lutites. Nature 299 (5885), 715–717.

Pan, R., Hou, T., Wang, X., Encarnación, J., Botcharnikov, R., 2022. Multiple magma storage regions and open system processes revealed by chemistry and textures of the Datong tholeiitic lavas, North China Craton. J. Petrol. 63 (5), egac034.

Peng, P., Zhai, M.G., Guo, J.H., Kusky, T., Zhao, T.P., 2007. Nature of mantle source contributions and crystal differentiation in the petrogenesis of the 1.78 Ga mafic dykes in the central North China craton. Gondwana Res. 12 (1–2), 29–46.

Pilet, S., Baker, M.B., Stolper, E.M., 2008. Metasomatized lithosphere and the origin of alkaline lavas. Science 320 (5878), 916–919.

Qian, S.P., Ren, Z.Y., Zhang, L., Hong, L.B., Liu, J.Q., 2015. Chemical and Pb isotope composition of olivine-hosted melt inclusions from the Hannuoba basalts, North China Craton: Implications for petrogenesis and mantle source. Chem. Geol. 401, 111–125.

Rapp, R.P., Irifune, T., Shimizu, N., Nishiyama, N., Norman, M.D., Inoue, T., 2008. Subduction recycling of continental sediments and the origin of geochemically enriched reservoirs in the deep mantle. Earth Planet. Sci. Lett. 271, 14–23.

Ren, Z.Y., Ingle, S., Takahashi, E., Hirano, N., Hirata, T., 2005. The chemical structure of the Hawaiian mantle plume. Nature 436 (7052), 837–840.

Rudnick, R.L., Fountain, D.M., 1995. Nature and composition of the continental crust: a lower crustal perspective. Rev. Geophys. 33 (3), 267–309.

Salters, V.J., Stracke, A., 2004. Composition of the depleted mantle. Geochem., Geophys., Geosyst. 5 (5).

Sato, H., 1977. Nickel content of basaltic magmas: identification of primary magmas and a measure of the degree of olivine fractionation. Lithos 10 (2), 113–120.

Sedaghatpour, F., Teng, F.Z., Liu, Y., Sears, D.W., Taylor, L.A., 2013. Magnesium isotopic composition of the Moon. Geochim. Cosmochim. Ac. 120, 1–16.

Shaw, J.E., Baker, J.A., Menzies, M.A., Thirlwall, M.F., Ibrahim, K.M., 2003. Petrogenesis of the largest intraplate volcanic field on the Arabian Plate (Jordan): a mixed lithosphere–asthenosphere source activated by lithospheric extension. J. Petrol. 44 (9), 1657–1679.

Sizova, E., Gerya, T., Brown, M., Perchuk, L.L., 2010. Subduction styles in the Precambrian: Insight from numerical experiments. Lithos 116 (3–4), 209–229.

Smith, E.I., Sanchez, A., Walker, J.D., Wang, K., 1999. Geochemistry of mafic magmas in the Hurricane Volcanic field, Utah: implications for small–and large–scale chemical variability of the lithospheric mantle. J. Geol. 107 (4), 433–448.

Søager, N., Portnyagin, M., Hoernle, K., Holm, P.M., Hauff, F., Garbe-Schönberg, D., 2015. Olivine major and trace element compositions in southern Payenia basalts, Argentina: evidence for pyroxenite–peridotite melt mixing in a back-arc setting. J. Petrol. 56 (8), 1495–1518.

Sobolev, A.V., Hofmann, A.W., Sobolev, S.V., Nikogosian, I.K., 2005. An olivine–free mantle source of Hawaiian shield basalts. Nature 434, 590–597.

Sobolev, A.V., Hofmann, A.W., Kuzmin, D.V., Yaxley, G.M., Arndt, N.T., Chung, S.L., Danyushevsky, L.V., Elliott, T., Frey, F.A., Garcia, M.O., Gurenko, A.A., Kamenetsky, V.S., Kerr, A.C., Krivolutskaya, N.A., Matvienkov, V.V., Nikogosian, I.K., Rocholl, A., Sigurdsson, I.A., Sushchevskaya, N.M., Teklay, M., 2007. The amount of recycled crust in sources of mantle–derived melts. Science 316, 412–417.

Song, Y., Frey, F.A., Zhi, X., 1990. Isotopic characteristics of Hannuoba basalts, eastern China: implications for their petrogenesis and the composition of subcontinental mantle. Chem. Geol. 88 (1–2), 35–52.

Stracke, A., Bourdon, B., 2009. The importance of melt extraction for tracing mantle heterogeneity. Geochim. Cosmochim. Ac. 73 (1), 218–238.

Su, B.X., Hu, Y., Teng, F.Z., Xiao, Y., Zhou, X.H., Sun, Y., Zhou, M.F., Chang, S.C., 2017. Magnesium isotope constraints on subduction contribution to Mesozoic and Cenozoic East Asian continental basalts. Chem. Geol. 466, 116–122.

Su, B.X., Hu, Y., Teng, F.Z., Xiao, Y., Zhang, H.F., Sun, Y., Yang, B., Zhu, B., Zhou, X.H., Ying, J.F., 2019. Light Mg isotopes in mantle–derived lavas caused by chromite crystallization, instead of carbonatite metasomatism. Earth Planet Sc. Lett. 522, 79–86.

Sun, S.S., McDonough, W.F., 1989. Chemical and isotopic systematics of oceanic basalts: implications for mantle composition and processes. In: Saunders, A.D., Norry, M.J. (Eds.), Magmatism in Ocean Basins. Geological Society of Special Publication, London, pp. 313–345.

Sun, Y., Teng, F.Z., Pang, K.N., 2021. The presence of paleo–Pacific slab beneath northwest North China Craton hinted by low-δ^{26}Mg basalts at Wulanhada. Lithos 386, 106009.

Tan, D.B., Xiao, Y., Dai, L.Q., Sun, H., Wang, Y., Gu, H.O., 2022. Differentiation between carbonate and silicate metasomatism based on lithium isotopic compositions of alkali basalts. Geology 50 (10), 1150–1155.

Tanaka, T., Togashi, S., Kamioka, H., Amakawa, H., Kagami, H., Hamamoto, T., Yuhara, M., Orihashi, Y., Yoneda, S., Shimizu, H., Kunimaru, T., Takahashi, K., Yanagi, T., Nakano, T., Fujimaki, H., Shinjo, R., Asahara, Y., Tanimizu, M., Dragusanu, C., 2000. JNdi–1: a neodymium isotopic reference in consistency with LaJolla neodymium. Chem. Geol. 168, 279–281.

Tang, Y.J., Zhang, H.F., Nakamura, E., Moriguti, T., Kobayashi, K., Ying, J.F., 2007. Lithium isotopic systematics of peridotite xenoliths from Hannuoba, North China Craton: implications for melt–rock interaction in the considerably thinned lithospheric mantle. Geochim. Cosmochim. Ac. 71 (17), 4327–4341.

Tang, Z.Y., Zhao, G.C., Zhang, M.X., Sun, D.Y., Zhang, C.L., Zhang, S.J., Sun, G.S., Zhang, Z.F., Shao, C., Yang, Y.C., Liu, C., Wang, X.P., 2022. Petrogenesis and tectonic affinity of Early Cretaceous potassic diorites in the northern Taihang Mountain, Trans-North China Orogen. J. Asian Earth Sci. 240, 105441.

Tatsumi, Y., Sakuyama, M., Fukuyama, H., Kushiro, I., 1983. Generation of arc basalt magmas and thermal structure of the mantle wedge in subduction zones. J. Geophys. Res.: Solid. Earth 88 (B7), 5815–5825.

Teng, F.Z., 2017. Magnesium isotope geochemistry. Rev. Mineral. Geochem. 82 (1), 219–287.

Teng, F.Z., Wadhwa, M., Helz, R.T., 2007. Investigation of magnesium isotope fractionation during basalt differentiation: implications for a chondritic composition of the terrestrial mantle. Earth Planet Sc. Lett. 261 (1–2), 84–92.

Teng, F.Z., Li, W.Y., Ke, S., Marty, B., Dauphas, N., Huang, S.C., Wu, F.Y., Pourmand, A., 2010. Magnesium isotopic composition of the Earth and chondrites. Geochim. Cosmochim. Ac. 74, 4150–4166.

Tian, Z.Y., Han, P., Xu, K.D., 1992. The Mesozoic-Cenozoic East China rift system. Tectonophysics 208 (1–3), 341–363.

Tian, H.C., Yang, W., Li, S.G., Ke, S., Chu, Z.Y., 2016. Origin of low δ^{26}Mg basalts with EM–I component: Evidence for interaction between enriched lithosphere and carbonated asthenosphere. Geochim. Cosmochim. Ac. 188, 93–105.

Tian, H.C., Yang, W., Li, S.G., Wei, H.Q., Yao, Z.S., Ke, S., 2019. Approach to trace hidden paleo-weathering of basaltic crust through decoupled Mg–Sr and Nd isotopes recorded in volcanic rocks. Chem. Geol. 509, 234–248.

Wang, X.J., Chen, L.H., Hofmann, A.W., Mao, F.G., Liu, J.Q., Zhong, Y., Xie, L.W., Yang, Y.H., 2017. Mantle transition zone–derived EM1 component beneath NE China: Geochemical evidence from Cenozoic potassic basalts. Earth Planet Sc. Lett. 465, 16–28.

Wang, X.J., Chen, L.H., Hofmann, A.W., Hanyu, T., Kawabata, H., Zhong, Y., Xie, L.W., Shi, J.H., Miyazaki, T., Hirahara, Y., Takahashi, T., Senda, R., Chang, Q., Vaglarov, B.S., Kimura, J.I., 2018. Recycled ancient ghost carbonate in the Pitcairn mantle plume. P. Natl. Acad. Sci. 115 (35), 8682–8687.

Wang, S.J., Li, S.G., 2022. Magnesium isotope geochemistry of the carbonate-silicate system in subduction zones. Natl. Sci. Rev. 9 (6), nwac036.

Wang, Z.Z., Liu, S.A., Ke, S., Liu, Y.C., Li, S.G., 2016. Magnesium isotopic heterogeneity across the cratonic lithosphere in eastern China and its origins. Earth Planet. Sci. Lett. 451, 77–88.

Wang, S.J., Teng, F.Z., Li, S.G., 2014. Tracing carbonate–silicate interaction during subduction using magnesium and oxygen isotopes. Nat. Commun. 5 (1), 5328.

Weinstein, Y., Navon, O., Altherr, R., Stein, M., 2006. The role of lithospheric mantle heterogeneity in the generation of Plio-Pleistocene alkali basaltic suites from NW Harrat Ash Shaam (Israel). J. Petrol. 47 (5), 1017–1050.

Whitaker, M.L., Nekvasil, H., Lindsley, D.H., Difrancesco, N.J., 2007. The role of pressure in producing compositional diversity in intraplate basaltic magmas. J. Petrol. 48 (2), 365–393.

White, W.M., 2010. Oceanic island basalts and mantle plumes: the geochemical perspective. Annu. Rev. Earth. Pl. Sc. 38, 133–160.

Wilson, M., Downes, H., 1991. Tertiary—Quaternary extension-related alkaline magmatism in western and central Europe. J. Petrol. 32 (4), 811–849.

Wu, L., Mei, L., Paton, D.A., Liu, Y., Guo, P., Shen, C., Liu, Z., Min, C., Li, M., 2020. Late Cretaceous-Cenozoic intraplate extension and tectonic transitions in eastern China: Implications for intraplate geodynamic origin. Mar. Petrol. Geol. 117, 104379.

Wu, F.Y., Walker, R.J., Ren, X.W., Sun, D.Y., Zhou, X.H., 2003. Osmium isotopic constraints on the age of lithospheric mantle beneath northeastern China. Chem. Geol. 196 (1–4), 107–129.

Xia, Q.X., Zhi, X.C., Meng, Q., Zheng, L., Peng, Z.C., 2004. The trace element and Re–Os isotopic geochemistry of mantle–derived peridotite xenoliths from Hannuoba: Nature and age of SCLM beneath the area. Acta Petrol. Sin. 20 (5), 1215–1224 (in Chinese with English abstract).

Xu, Y., Li, H., Pang, C., He, B., 2009. On the timing and duration of the destruction of the North China Craton. Chinese Sci. Bull. 54 (19), 3379–3396.

Xu, Y., Li, H., Hong, L., Ma, L., Ma, Q., Sun, M., 2018. Generation of Cenozoic intraplate basalts in the big mantle wedge under eastern Asia. Sci. China Earth Sci. 61 (7), 869–886.

Xu, Z., Zheng, Y.F., 2017. Continental basalts record the crust–mantle interaction in oceanic subduction channel: A geochemical case study from eastern China. J. Asian Earth Sci. 145, 233–259.

Yan, Q., Shi, X., Metcalfe, I., Liu, S., Xu, T., Kornkanitnan, N., Sirichaiseth, T., Yuan, L., Zhang, Y., Zhang, H., 2018. Hainan mantle plume produced late Cenozoic basaltic rocks in Thailand. Southeast Asia. Sci. Rep. 8 (1), 1–14.

Yang, C., Liu, S.A., 2019. Zinc isotope constraints on recycled oceanic crust in the mantle sources of the Emeishan large igneous province. J. Geophys. Res.: Solid. Earth 124 (12), 12537–12555.

Yang, W., Teng, F.Z., Zhang, H.F., Li, S.G., 2012. Magnesium isotopic systematics of continental basalts from the North China craton: Implications for tracing subducted carbonate in the mantle. Chem. Geol. 328, 185–194.

Young, E.D., Galy, A., 2004. The isotope geochemistry and cosmochemistry of magnesium. Rev. Mineral. Geochem. 55, 197–230.

Zeng, G., Chen, L.H., Xu, X.S., Jiang, S.Y., Hofmann, A.W., 2010. Carbonated mantle sources for Cenozoic intra–plate alkaline basalts in Shandong. North China. Chem. Geol. 273 (1–2), 35–45.

Zeng, G., Chen, L.H., Hofmann, A.W., Wang, X.J., Liu, J.Q., Yu, X., Xie, L.W., 2021. Nephelinites in eastern China originating from the mantle transition zone. Chem. Geol. 576, 120276.

Zhai, M.G., Santosh, M., Zhang, L., 2011. Precambrian geology and tectonic evolution of the North China Craton. Gondwana Res. 20 (1), 1–5.

Zhang, Y., Chen, L., Ai, Y., Jiang, M., Xu, W., Shen, Z., 2018. Lithospheric structure of the South China Block from S–receiver function. Chin. J. Geophys. 61, 138–149 (in Chinese with English abstract).

Zhang, W.H., Zhang, H.F., Fan, W.M., Han, B.F., Zhou, M.F., 2012. The genesis of Cenozoic basalts from the Jining area, northern China: Sr–Nd–Pb–Hf isotope evidence. J. Asian Earth Sci. 61, 128–142.

Zhao, D., 2021. Seismic imaging of Northwest Pacific and East Asia: New insight into volcanism, seismogenesis and geodynamics. Earth-Sci. Rev. 214, 103507.

Zhao, G., Cawood, P.A., Wilde, S.A., Sun, M., Lu, L., 2000. Metamorphism of basement rocks in the Central Zone of the North China Craton: implications for Paleoproterozoic tectonic evolution. Precambrian Res. 103 (1–2), 55–88.

Zheng, X., 1985. Meso-Cenozoic volcanic rocks in east China and adjacent areas with relation to plate tectonics. Tectonophysics 112 (1–4), 533–550.

Zheng, J., Xia, B., Dai, H., Ma, Q., 2021. Lithospheric structure and evolution of the North China Craton: An integrated study of geophysical and xenolith data. Sci. China Earth Sci. 64 (2), 205–219.

Zhong, Y., Chen, L.H., Wang, X.J., Zhang, G.L., Xie, L.W., Zeng, G., 2017. Magnesium isotopic variation of oceanic island basalts generated by partial melting and crustal recycling. Earth Planet Sc. Lett. 463, 127–135.

Zhu, R., Xu, Y., Zhu, G., Zhang, H., Xia, Q., Zheng, T., 2012. Destruction of the North China craton. Sci. China Earth Sci. 55 (10), 1565–1587.

Zindler, A., Hart, S.R., 1986. Chemical geodynamics. Annu. Rev. Earth Planet. Sci. 14, 493–571.

Zou, H., Fan, Q., Yao, Y., 2008. U-Th systematics of dispersed young volcanoes in NE China: asthenosphere upwelling caused by piling up and upward thickening of stagnant Pacific slab. Chem. Geol. 255 (1–2), 134–142.

Zou, Z., Wang, Z., Foley, S., Xu, R., Geng, X., Liu, Y.N., Liu, Y., Hu, Z., 2022. Origin of low–MgO primitive intraplate alkaline basalts from partial melting of carbonate–bearing eclogite sources. Geochim. Cosmochim. Ac. 324, 240–261.